

## CHARACTERIZATION OF NATURAL FELDSPARS BY RAMAN SPECTROSCOPY FOR FUTURE PLANETARY EXPLORATION

JOHN J. FREEMAN<sup>§</sup>, ALIAN WANG, KARLA E. KUEBLER,  
 BRADLEY L. JOLLIFF AND LARRY A. HASKIN<sup>†</sup>

*Department of Earth and Planetary Sciences and McDonnell Center for Space Sciences,  
 Washington University in St. Louis, St. Louis, Missouri 63130, U.S.A.*

### ABSTRACT

The Raman spectra of a large number of natural feldspar-group minerals were obtained to determine what compositional and structural information can be inferred solely from their Raman spectra. The feldspar minerals selected cover a wide range of Na, K, and Ca proportions, crystal structures and degrees of cation disorder. The samples include both homogeneous feldspar phases and a few with visible intergrowths. From the positions of the strongest Raman peak in the spectrum, four structural types of feldspars can be readily identified: orthoclase (and microcline), albite, high-temperature plagioclase, and anorthite. Using a Raman spectral database of feldspar minerals established during this study and an autonomous spectral search-and-match routine, up to seven different types of feldspar can be unambiguously determined. Three additional feldspar types can be further resolved by careful visual inspection of the Raman spectra. We conclude that ten types of feldspars can be classified according to their structure, crystallinity, and chemical composition solely on the basis of their Raman spectra. Unlike olivine, pyroxene and some Fe-oxides, the Raman peak positions of the feldspars cannot be used to extract quantitative information regarding the cation composition of the feldspar phases. We also define the necessary specifications of a field Raman spectrometer capable of characterizing feldspar minerals during planetary surface exploration.

*Keywords:* Raman spectroscopy, feldspar-group minerals, mineralogy, planetary spectroscopy.

### SOMMAIRE

Nous avons déterminé le spectre Raman d'un grand nombre de minéraux du groupe des feldspaths afin d'établir quel type d'information compositionnelle et structurale peut en découler. Les échantillons choisis couvrent une grande étendue en termes de proportions de Na, K, et Ca, de structures cristallines et de désordre parmi les cations. Parmi eux se trouvent des échantillons homogènes et quelques-uns ayant des intercroissances visibles. D'après la position des pics principaux du spectre Raman, nous pouvons facilement identifier quatre types de structure: orthoclase (et microcline), albite, plagioclase de haute température et anorthite. Au moyen d'une banque de spectres Raman des minéraux du groupe des feldspaths, établie pendant notre étude, et un logiciel autonome permettant des recherches et des comparaisons, on peut identifier jusqu'à sept types distincts de feldspath sans ambiguïté. On peut en plus résoudre trois types additionnels par inspection visuelle soignée des spectres. Nous croyons qu'il est possible de classer dix sortes de feldspaths selon leur structure, cristallinité, et composition chimique uniquement en utilisant leur spectre Raman. Contrairement au cas de l'olivine, du pyroxène et de certains oxydes de fer, la position des pics du spectre ne peut pas fournir de l'information quantitative à propos de la composition des feldspaths examinés. Nous définissons aussi les spécifications requises pour un spectromètre Raman de terrain capable de caractériser les feldspaths lors de l'exploration d'une surface planétaire.

(Traduit par la Rédaction)

*Mots-clés:* spectroscopie Raman, minéraux du groupe des feldspaths, minéralogie, spectroscopie planétaire.

<sup>§</sup> E-mail address: johnjfreeman@wustl.edu

## INTRODUCTION

Feldspar-group minerals are framework silicates and among the most common rock-forming minerals of planetary crusts. On Earth, they occur in many types of igneous, metamorphic and sedimentary rocks. On the Moon, plagioclase is the most abundant mineral. Feldspars are one of the main minerals in martian meteorites and have been identified as a widespread component of basaltic rocks on the martian surface by the Thermal Emission Spectrometer (TES) on the Mars Global Surveyor (Bandfield *et al.* 2000, Bandfield 2002, Christensen *et al.* 2000, 2001, Larsen *et al.* 2000, Ruff & Christensen 2002). Maskelynite, a shock-vitrified feldspar, is present in martian meteorites found on Earth (Cooney *et al.* 1999, Papike *et al.* 2003, Rubin 1997, Sautter *et al.* 2002, Taylor *et al.* 2002, Wang *et al.* 1999, Xirouchakis *et al.* 2002). Feldspar-group minerals also have been identified in numerous rocks and soils at the landing sites of the Mars Exploration Rovers (MER) (McSween *et al.* 2004, Clark *et al.* 2005, Squyres *et al.* 2006, Ming *et al.* 2006, Wang *et al.* 2006, Jolliff *et al.* 2006a, Schröder *et al.* 2008).

Our motivation in this work is to determine the Raman spectral characteristics of the feldspar-group minerals that can be used to distinguish them and the accuracy needed to make these distinctions with a portable or remotely deployed instrument. The availability in the last decade of improved Raman instrumentation using small, stable, intense lasers, high-performance optical filters, sensitive CCD array detectors and advanced, fast grating systems has enabled us to develop the Mars Microbeam Raman Spectrometer (MMRS), a portable field Raman spectrometer (Wang *et al.* 2003) suitable for surface exploration on Mars. This field instrument has the precision and accuracy to yield Raman spectra with enough resolution to identify many minerals, including crystal-structure information, and estimates of cation proportions of common igneous minerals such as olivine, pyroxene, phosphates, spinels, and Fe–Ti oxides (Kuebler *et al.* 2006, Wang *et al.* 2001, 2004a, b, Jolliff *et al.* 2006b).

The purpose of the present study is to generate an internally consistent set of Raman spectra from a wide variety of natural feldspar-group minerals of known composition and structure. The compositions of minerals were determined, as needed, with electron-microprobe (EMP) analyses, and the aspects of the structure of a few samples were verified by powder X-ray diffraction (XRD). The Raman spectral differences are linked to the structural and compositional characteristics of the feldspars. A database established with the Raman spectra collected in this study was used to test correlations between peak positions and cation ratios of the intermediate feldspar compositions as well as changes in spectral pattern with structural distortions such as cation disorder and reduced crystallinity. Finally, we evaluate the experimental conditions and instrumental

requirements of a field-portable Raman system capable of distinguishing different varieties of feldspar likely to be found in planetary surface materials.

## BACKGROUND INFORMATION

Past and ongoing planetary missions (including orbiters, landers, and rovers) all provide bulk chemical and spectral characteristics, *i.e.*, spectral signatures representing all of the minerals within the field of view (FOV) ranging from the centimeter scale on the rovers to hundreds of meters on the orbiting spacecraft. The individual mineral phases within the FOV and their characteristics are deduced through spectral deconvolution or model analyses of the data obtained from the mixture. By comparison, our laboratory Raman microprobe spectrometer and the MMRS examine a small area of the sample, ranging in size from a few micrometers for the lab instrument to ~20  $\mu\text{m}$  for the MMRS, permitting us in most cases to measure individual grains within a heterogeneous sample. Information on chemical zoning, mineral assemblages and rock texture can be obtained by collecting spectra at regular distance intervals (Raman point counting, Haskin *et al.* 1997) across the surface of the sample. On the basis of our earlier studies, we can readily detect feldspar-group minerals in the presence of other types of silicates using Raman spectroscopy, and some varieties can be distinguished (Matson *et al.* 1986, Sharma *et al.* 1983). We wish to demonstrate, however, the full capacity of Raman spectroscopy for the characterization of the feldspars in which the overall range of peak positions is relatively limited.

There are numerous publications concerning the Raman spectra of various feldspar-group minerals (Daniel 1995a, b, Frogner 1998, Heymann & Hörz 1990, Matson *et al.* 1986, McKeown 2005, Mernagh 1991, Purcell & White 1983, Salje 1986, Sharma *et al.* 1983, von Stengel 1977, Velde & Boyer 1985, Velde *et al.* 1989). The literature to date on the Raman spectra of these feldspars indicates that feldspars with different structures and compositions can be distinguished by their Raman spectral patterns. Mernagh (1991) has shown that alkali feldspars are easily distinguished from plagioclase using only the position of the strongest Raman peak. He concluded that the feldspars within these two groups could be further distinguished by more detailed analysis of their Raman spectra, but did not elaborate on this conclusion.

The Raman spectra of the feldspars reported over the last 35 years have been acquired with Raman spectrometers of different generations, with different spectral resolutions and varying degrees of accuracy in wavenumber. These instrumental variations complicate comparison of Raman spectral features of feldspars discussed in different publications. Inconsistencies in the published data quickly became apparent when we attempted to use the literature referenced above to

determine how many of the different feldspar phases within the alkali or plagioclase subgroups could be characterized by their Raman spectra.

## EXPERIMENTAL

### *Feldspar samples*

A total of 32 samples of feldspar-group minerals were characterized by Raman spectroscopy for this study. These samples cover a broad range of feldspar types, including compositional end-members, intermediate compositions, and structures having differing degrees of cation order, as well as one produced by shock impact. A list of the samples studied is shown in Table 1 and displayed in the triangular diagram (Fig. 1). These samples fall into three categories based on prior knowledge of their identities:

#### *(1) Well-characterized samples*

Raman spectra obtained from these samples were found to match published Raman spectra of the same type of feldspar from same or different localities, where the publication cited included both structural and chemical characterizations of the mineral. We considered the identities of these samples as confirmed, with no additional EMP or XRD analyses needed for characterization.

#### *(2) Samples needing further chemical characterization*

Our Raman spectra taken from these samples matched Raman spectra of the same types of feldspars shown in one or more publications, but authors of those publications did not supply supporting chemical and structural data. Many of our samples fall into this category, and we conducted EMP analyses on them. Once we obtained a chemical composition and Raman spectrum of a sample that matched a published Raman spectrum with supporting XRD data, we considered the structure and identity of the sample to be confirmed.

#### *(3) Samples needing both chemical and structural characterization*

Six of our samples either had Raman spectra that conflicted with published Raman spectra, or were a type of feldspar for which there was no published Raman spectrum. We determined the compositions and structures of these samples using EMP and XRD analyses.

### *Raman spectroscopic analyses*

Raman spectra were collected with a HoloLab 5000 Raman microprobe spectrometer system (Kaiser Optical Systems, Inc., KOSI). This system employs the 532

nm, frequency-doubled, Nd:YAG solid-state laser as the excitation source and a holographic grating spectrometer covering the Raman Stokes shift range of  $\sim 0$  to  $4300\text{ cm}^{-1}$  relative to the 532 nm laser line. The spectrometer has a spectral resolution of  $4\text{--}5\text{ cm}^{-1}$  and uses a  $256 \times 2048$  pixel array CCD camera for recording Raman spectra. The 532 nm laser radiation is sent through a single-mode optical fiber ( $\sim 8\text{ }\mu\text{m}$  in diameter) into a probe head attached to the optical microscope of the KOSI microprobe system. A microscope objective condenses the laser beam onto the sample and collects the back-scattered Raman signal. The Raman signal is returned to the spectrograph through a multimode optical fiber ( $100\text{ }\mu\text{m}$  in diameter) without the use of a depolarizer. The optical microscope is also used for viewing and photographing the sample with either transmitted or reflected light. Two objectives were used in this Raman study: (a) a  $20\times$  (NA 0.4) with a working distance of 12 mm that produces a beam diameter of  $\sim 6\text{ }\mu\text{m}$  at focus, and (b) a  $50\times$  (NA 0.75) with working distance of 0.5 mm that produces a beam diameter of  $\sim 2\text{ }\mu\text{m}$  at focus. The power of the laser beam at the sample was measured to be  $\sim 13\text{ mW}$ . As laser light traveling through a single-mode excitation fiber is partially polarized, the recorded intensities of Raman peaks in some of the Raman bands generated from a single-crystal specimen may depend on the orientation of the crystal axes of the sample with respect to the plane of polarization of the excitation laser beam. The Raman analyses were made on either loose grains of feldspar without any sample preparation, or on the polished surfaces of feldspar grains prepared for the EMP study. Collection times of the spectra ranged from  $<1$  minute to 15 minutes, depending upon sample size, Raman scattering efficiency, and the intensity (if any) of background fluorescence.

Wavelength and intensity calibrations of the CCD camera were made with a neon emission spectral calibration lamp and a NIST secondary standard white light, a light source supplied in the KOSI accessory kit HCA-0095. The zero Raman-shift frequency of the excitation laser was calibrated daily before acquiring any sample spectra by measuring the Raman peak position of single crystal of silicon ( $520.7\text{ cm}^{-1}$ ). Occasionally, the  $1001.5\text{ cm}^{-1}$  Raman band of polystyrene or the  $801.8\text{ cm}^{-1}$  Raman band of liquid cyclohexane also were used. These calibrations ensured that measurement errors on Raman peak positions were less than  $\pm 1\text{ cm}^{-1}$ .

### *Electron-microprobe analyses*

Individual grains were prepared for correlated Raman and electron-microprobe (EMP) analysis by mounting them in epoxy on glass slides and polishing the surfaces down to  $0.25\text{ }\mu\text{m}$  grit. Several Raman spectra were acquired from each polished surface before carbon coating the sample for EMP analysis.

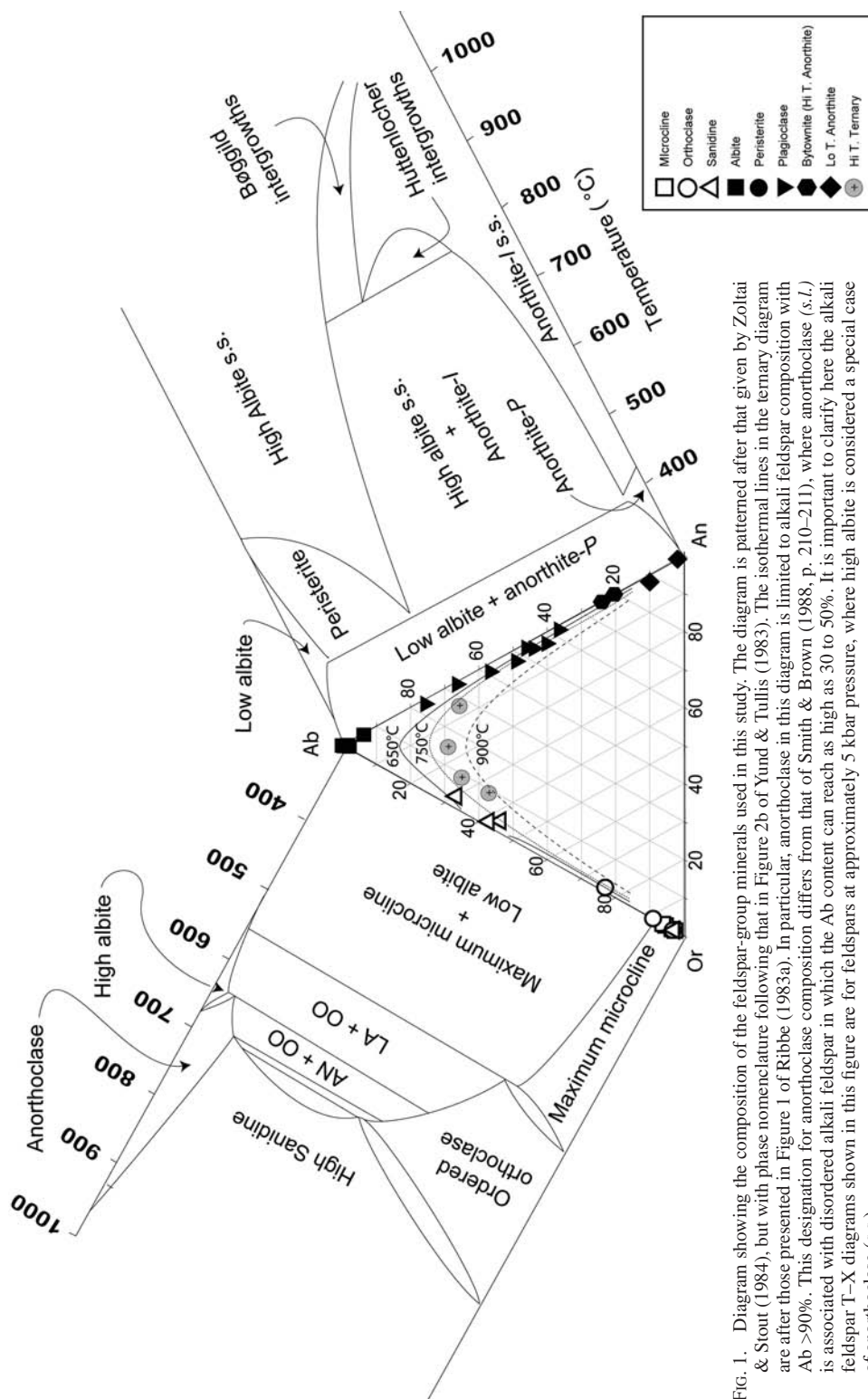


FIG. 1. Diagram showing the composition of the feldspar-group minerals used in this study. The diagram is patterned after that given by Zoltai & Stout (1984), but with phase nomenclature following that in Figure 2b of Yund & Tullis (1983). The isothermal lines in the ternary diagram are after those presented in Figure 1 of Ribbe (1983a). In particular, anorthoclase in this diagram is limited to alkali feldspar composition with Ab >90%. This designation for anorthoclase composition differs from that of Smith & Brown (1988, p. 210–211), where anorthoclase (s.l.) is associated with disordered alkali feldspar in which the Ab content can reach as high as 30 to 50%. It is important to clarify here the alkali feldspar T-X diagrams shown in this figure are for feldspars at approximately 5 kbar pressure, where high albite is considered a special case of anorthoclase (s.s.).

TABLE 1. FIELD SAMPLES OF FELDSPARS EMPLOYED IN THIS STUDY

Sample label	Collector or sample #	Location where collected	Feldspar phases detected
Microcline	EPSc #313	Crystal Peak, Colorado	Microcline
Microcline	AW #162	Haicheng, Liaoning, China	Microcline, albite
Microcline	EPSc #1	Black Hills, South Dakota	Microcline, albite
Microcline, adularia habit, var. moonstone,	EPSc #313-4	Meconite, New York	Microcline, albite
Microcline	JDP #109940	Lake George, Colorado	Microcline, orthoclase, albite, disordered albite
Microcline,	ASU BUR-3460A	Keystone, South Dakota	Microcline, albite
Orthoclase	JDP Sierra de Palo Dulce	Sierra de Palo Dulce, Guerrero, Mexico	Orthoclase
Orthoclase, var. adularia	EPSc #313-10	St. Gothard, Switzerland	Orthoclase, albite
Labradorite*	ASU H314.4b	(not available)	Orthoclase, sanidine, oligoclase
Glassy tablet in welded volcanic pumice	RO welded pumice	Bandelier National Monument, New Mexico	Sanidine
Glassy tablet in non- welded volcanic pumice	RO unwelded pumice	Bandelier National Monument, New Mexico	Sanidine
Anorthoclase	AW #465	Anhui, China	Sanidine
Anorthoclase	AW #164	Jiashan, Anhui, China	Sanidine
Albite	JDP Albite	Amelia Court House, Virginia	Albite
Albite	AW #162	Haicheng, Liaoning, China	Albite, microcline
Peristerite	JDP #10-997	Eganville, Ontario, Canada	Albite
Grey Anorthosite	RD Grey Anorthosite	Montpellier, Virginia	Andesine
Labradorite	AW #3-8	(not available)	Andesine
Pink Anorthosite	RD #LC002-14088	Lac Chaudière, Quebec, Canada	Andesine, sanidine
Anorthite	AW #C-3	(not available)	Andesine
Labradorite	ASU WAR-4524	Lac St-Jean, Quebec, Canada	Labradorite
Labradorite, ASU	ASU BUR-3080A	Essex County, New York	Labradorite
Anorthite	AW #3-14	(not available)	Andesine
Labradorite, Bøggild intergrowths	RD #PG721	Nain, Labrador, Canada	Labradorite
Plagioclase	AW #85-5-20	(not available)	Labradorite
Black anorthosite	RD #LSJ 80-192	Lac St. Jean, Quebec, Canada	Labradorite
Plagioclase, Huttenlocher intergrowths	RD #OGG-138	Buksefjord, Greenland	Bytownite [high (I) anorthite]
Lunar cataclastic plagioclase	NASA <sup>§</sup> 67513, 7075	Station 11, North Ray Crater, Apollo 16 landing site	Low (P) anorthite
Plagioclase crystal in thin section	NHML ** NWA 773	Lunar meteorite found in northwestern Africa	Shocked anorthite
Trachyte	EPSc #27-32	Drachenfels, near Bonn, Prussia, Germany	Sanidine, ternary feldspar
Crystal in volcanic glass	ND	Mount Erebus, Antarctica	Ternary feldspar
Anorthoclase	ASU WAR-0579	Larvik, Norway	Ternary feldspar

EPSc: Mineral collection of the Department of Earth & Planetary Sciences, Washington University in St. Louis. AW: Personal collection of Dr. Alian Wang, Department of Earth & Planetary Sciences, Washington University in St. Louis. JDP: Personal collection of Prof. Jill D. Pasteris, Department of Earth & Planetary Sciences, Washington University in St. Louis. ASU: Mineral collection of the Arizona State University Mars Thermal Emission Spectrometer Project. RO: Personal collection of Robert Osburn, Department of Earth & Planetary Sciences, Washington University in St. Louis. RD: Personal collection of Prof. Robert Dymek, Department of Earth & Planetary Sciences, Washington University in St. Louis. <sup>§</sup> 67513: lunar sample collection (U.S. government) as described Jolliff & Haskin (1995). \* Sample label does not agree with detected phases. \*\* We thank Monica Grady and the Natural History Museum of London for providing samples of NWA773. We are grateful to Marvin Killgore for making portions of this meteorite available to the scientific community for study. The sample is fully described Jolliff *et al.* (2003). <sup>†</sup> From the collection of Dr. Nella Dunbar, New Mexico Bureau of Geology & Mineral Resources, as described by Dunbar (1994).

The Raman sample locations were photo-documented so that the same spot could be relocated using recognizable microscopic features for EMP analysis. The EMP analyses were made on a JEOL 733 Superprobe equipped with three-wavelength dispersive spectrometers, a back-scattered electron (BSE) detector and Advanced Microbeam™ automation. We used an

accelerating voltage of 15 kV, a beam current of 20 nA, and a defocused beam (10 µm spot size) to prevent volatilization of Na. Several EMP analyses were taken to gauge sample heterogeneity and characterize exsolution features. We used a combination of feldspar and silicate standards to calibrate and monitor the EMP data collection. A modified Armstrong (1988) CITZAF routine



incorporated into the electron-microprobe software was used for X-ray matrix corrections. Molar proportions of the cations were calculated from the measured weight percentages of the corresponding oxides on the basis of eight oxygen atoms per unit formula.

### *XRD powder-diffraction analyses*

For six of the feldspar samples, several small pieces of each sample were hand ground with a mortar and pestle, dried as a slurry onto glass slides, and run as randomly oriented powder mounts for XRD. Analyses were made on a wide-angle Rigaku Geigerflex D-MAX/A diffractometer using CuK $\alpha$  radiation (35 kV, 35 mA) having a Bragg–Brentano focusing geometry with a 1° incident aperture slit, a 0.8° detector slit and a scintillation counter as the detector. We used a 2 $\theta$  range of 4–70°, a 2 $\theta$  step size of 0.04°, and a one-second dwell time per step. The data were collected and reduced using the Jade software (version 3.1, Materials Data, Inc., Livermore, California).

## RESULTS

Experimentally determined XRD powder-diffraction patterns represent an averaged sum of the diffraction of the individual phases in the powdered sample. On the other hand, with the EMPA and Raman microprobe techniques, one is generally able to analyze single phases resolvable at optical microscopic scales ( $\leq 10$   $\mu\text{m}$ ). Among the 32 mineral samples selected for this study, nine showed two or more optically resolvable feldspar phases. By correlating the locations of the Raman sampling spots with those of the EMP analyses, we were able to obtain information regarding both the composition and structure at the same sample spot. We, however, were not able to resolve the compositional and Raman spectral differences of the submicrometric textures displayed by the cryptoperthite, peristerite and Bøggild and Huttenlocher intergrowths (Ribbe 1983a).

For the study presented here, a total of 170 Raman spectra, 213 EMP analyses, and six XRD analyses were obtained from 42 different feldspar phases (belonging to 11 varieties of feldspar) occurring in the 32 feldspar samples investigated. Table 2 lists the EMP and Raman data from eleven unique samples averaged over multiple locations in a given phase. Also included are the positions of the five characteristic Raman peaks. Table 2 also lists the standard deviations for both the EMP and Raman data arising from minor compositional variations within a single phase and from instrumental error. In Table 3, we present the averaged values for Raman peak positions, the end-member compositions, and the XRD powder-diffraction results on those six samples needing structural confirmation.

In both Tables 2 and 3, the feldspar samples are ordered first by structural type and then by composition.

A triangular composition diagram showing the distribution of the compositions and structures of the feldspar phases encountered in this study is shown as Figure 1. Attached to the phase diagram for the ternary system are the secondary temperature–composition diagrams for the alkali (K, Na feldspar) and plagioclase (Na, Ca feldspar) joins. These diagrams are included to show the correlation between recognized feldspar structures and concentrations of the main cations, K<sup>+</sup>, Na<sup>+</sup> and Ca<sup>2+</sup>. These phase diagrams also show the feldspar nomenclature adopted for this study: **Or** for orthoclase, the K<sup>+</sup> end-member, **Ab** for albite, the Na<sup>+</sup> end-member, and **An** for anorthite, the Ca<sup>2+</sup> end-member. [Whereas the use of Or (for orthoclase *s.l.*) To designate the potassic end-member of the feldspar diagram is common, it is not to be confused with the orthoclase (*s.s.*) structural phase, which is a partially disordered, high-temperature K-feldspar.] We also use the following standard nomenclature for the high-temperature plagioclases: oligoclase: An<sub>10–30</sub>, andesine: An<sub>30–50</sub>, labradorite: An<sub>50–70</sub>, bytownite: An<sub>70–90</sub>, anorthite: An<sub>90–100</sub>, and ternary feldspars for phases exhibiting significant amounts of all three cations.

## DISCUSSION

### *General Raman spectral features of feldspar*

The tectosilicate structure with fully linked tetrahedra produces a Raman spectral pattern distinctly different from those of ortho-, chain, ring and layer silicates, in which the TO<sub>4</sub> tetrahedra are not linked at all, or only partially linked, with other TO<sub>4</sub> units (Deer *et al.* 1991). The strongest Raman peak in the tectosilicate spectrum is located below 600 cm<sup>−1</sup>, and in many instances this feature can be used to identify the specific tectosilicate. The Raman spectral features of the feldspars (crystal structure shown in Fig. 2) are distinctly different from those of other tectosilicates such as quartz and zeolites (Sharma *et al.* 1983, Matson *et al.* 1986). In particular, the Raman spectra of the feldspars are readily recognized by the presence of two or three Raman peaks lying between 450 and 515 cm<sup>−1</sup>, the strongest of which falls within the narrow region of 505 to 515 cm<sup>−1</sup> (Fig. 3). The peak position of the strongest Raman band of many tectosilicates shows an inverse correlation with the size of the ring made by the TO<sub>4</sub> tetrahedra. For example, quartz has a six-membered ring, and its strongest Raman peak occurs at 464 cm<sup>−1</sup>; LiAlSi<sub>2</sub>O<sub>6</sub>-II has a five-membered ring subunit, and its strongest Raman peak is at 492 cm<sup>−1</sup>, whereas feldspars, with a four-membered ring, show the strongest Raman peak to be near ~510 cm<sup>−1</sup> (Sharma *et al.* 1983).

In this paper, we separate the feldspar spectral characteristics as follows (Fig. 3): Group-I peaks occur in the spectral region of 450–520 cm<sup>−1</sup>, Group-II peaks, between 200 and 400 cm<sup>−1</sup>, Group-III peaks, below 200 cm<sup>−1</sup>, Group-IV peaks, between 600 and 800 cm<sup>−1</sup>, and

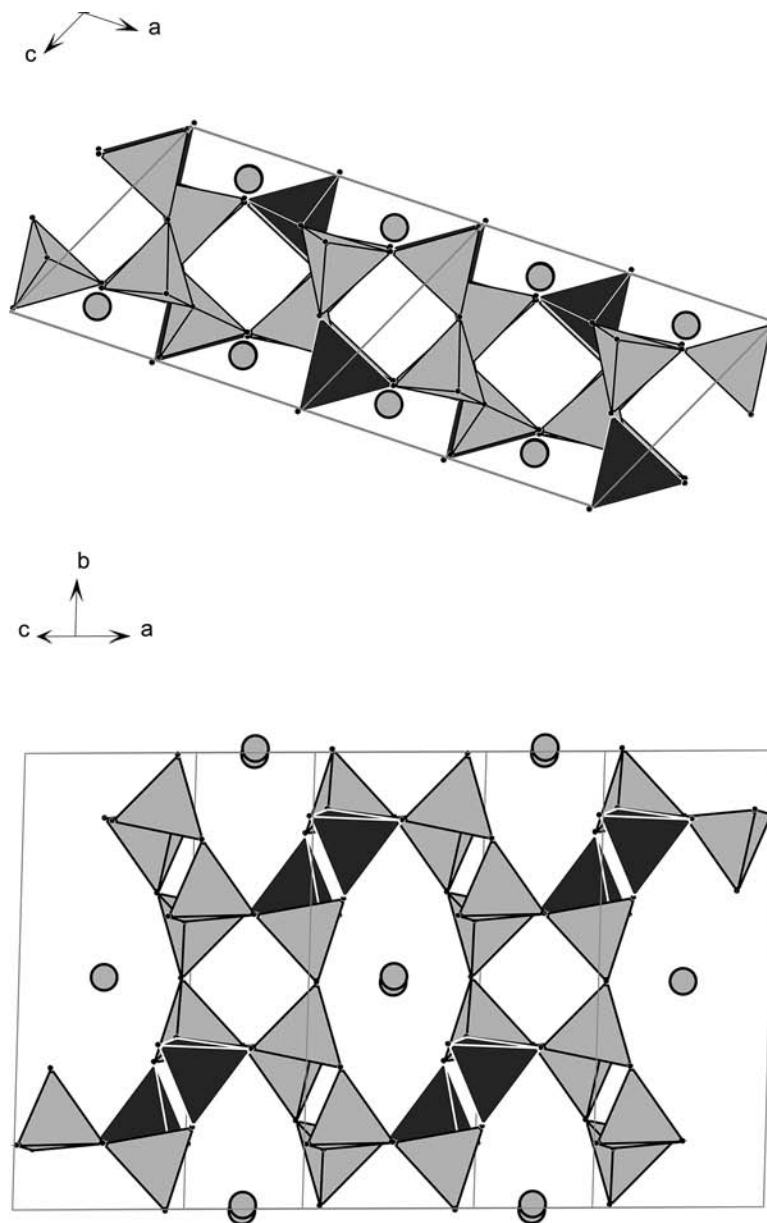


FIG. 2. Unit-cell structure of a typical feldspar, maximum microcline. Aluminum-bearing tetrahedra shaded in dark grey, silicon-bearing tetrahedra shaded in light grey, and potassium ions represented by circles. Two unit cells ( $2 \times 1 \times 1$ ) are shown.

Group-V peaks, between  $900$  and  $1200\text{ cm}^{-1}$ . Positions of all these peaks for 14 typical feldspar samples are listed in Table 4, whereas the average positions of the five strongest Raman peaks:  $I_a$ ,  $I_b$ , and  $I_c$  of Group I, and the strongest peak in Group II ( $II_{\max}$ ) and Group III

( $III_{\max}$ ) are listed in Tables 2 and 3, together with EMP and XRD data. The peaks in Groups IV and V will be discussed later, but these moderate- to weak-intensity Raman peaks are commonly obscured by the spectra of other silicates and anionic salts present in soil and

TABLE 2. ELECTRON-MICROPROBE AND RAMAN CHARACTERIZATION OF ELEVEN UNIQUE FELDSPAR PHASES

Phase <i>n</i> *	Microcline 9	Orthoclase 5	Sanidine 6	Albite 4	Low albite 10	Oligoclase 2	Andesine 13	Labradorite 7	Anorthite- <i>I</i> 10	Anorthite- <i>P</i> 3	Shocked anorthite NHML NWA #773											
Field sample	EPSc #313	ASU HS314.4b	Glassy tablet in welded pumice	AW 162	Peristerite 10-997	ASU HS314.4b	anorthosite LC002- 14088	PG721 Bøggild intergrowths	RD #OGG- 138	NASA 67513, 7075												
	Avg. $\pm\sigma$	Avg. $\pm\sigma$	Avg. $\pm\sigma$	Avg. $\pm\sigma$	Avg. $\pm\sigma$	Avg. $\pm\sigma$	Avg. $\pm\sigma$	Avg. $\pm\sigma$	Avg. $\pm\sigma$	Avg. $\pm\sigma$												
K <sub>2</sub> O wt.%	16.68	0.27	13.17	1.38	8.06	1.73	0.06	0.01	0.40	0.09	0.45	0.09	0.01	0.004	0.02	0.00	0.15	n.d.				
Na <sub>2</sub> O	0.30	0.14	2.15	0.75	6.52	0.22	11.13	0.16	10.28	0.17	8.76	0.10	6.46	0.23	5.02	0.10	2.34	0.06	0.59	n.d.		
FeO	0.03	0.06	0.11	0.07	0.05	0.08	0.03	0.04	0.06	0.03	0.07	0.05	0.14	0.05	0.25	0.04	0.02	0.03	0.01	0.39	n.d.	
CaO	0.00	0.005	0.23	0.21	0.73	0.65	1.26	0.39	2.57	0.15	4.84	0.31	8.46	0.42	11.05	0.16	16.50	0.26	19.75	0.13	18.83	n.d.
Al <sub>2</sub> O <sub>3</sub>	18.72	0.18	18.78	0.53	18.94	0.34	20.73	0.45	21.92	0.26	23.53	0.35	26.88	0.45	28.44	0.32	34.00	0.14	35.89	0.19	34.65	n.d.
SiO <sub>2</sub>	63.26	0.59	63.25	1.88	65.88	0.83	66.46	0.47	65.23	0.84	61.53	0.26	56.84	0.74	54.63	0.40	48.53	0.36	43.43	0.41	45.20	n.d.
MgO	0.00	0.004	0.01	0.01	0.01	0.01	0.00	0.00	0.01	0.00	0.01	0.01	0.01	0.01	0.01	0.01	0.01	0.01	0.01	0.11	n.d.	
TiO <sub>2</sub>	0.03	0.05	0.02	0.03	0.18	0.35	0.09	0.02	0.08	0.07	0.04	0.04	0.04	0.06	0.06	0.05	0.01	0.02	n.d.	n.d.	n.d.	n.d.
BaO	0.03	0.02	0.70	0.21	1.19	2.20	0.02	0.02	0.08	0.14	0.04	0.04	0.10	0.18	0.02	0.02	0.02	0.02	n.d.	n.d.	n.d.	n.d.
MnO	0.01	0.01	0.01	0.02	0.54	0.59	0.03	0.05	0.03	0.03	0.01	0.01	0.03	0.04	0.00	0.01	0.03	0.02	n.d.	n.d.	n.d.	n.d.
SrO	0.00	0.00	0.00	0.00	0.21	0.34	0.00	0.00	0.00	0.00	0.00	0.00	0.00	0.00	0.00	0.00	0.00	0.00	n.d.	n.d.	n.d.	n.d.
Total	99.05	0.57	98.43	2.88	102.29	4.24	99.82	0.67	100.65	0.87	99.05	0.69	99.34	0.67	99.92	0.35	101.46	0.27	99.45	0.28	99.92	n.d.
K <i>apfu</i>	0.998	0.015	0.786	0.075	0.459	0.096	0.003	0.001	0.022	0.005	0.013	0.012	0.02	0.01	0.026	0.005	0.001	0.000	0.001	0.000	0.009	n.d.
Na	0.027	0.012	0.196	0.068	0.566	0.013	0.949	0.016	0.874	0.015	0.761	0.007	0.57	0.02	0.440	0.010	0.205	0.015	0.024	0.005	0.053	n.d.
Fe	0.001	0.002	0.004	0.003	0.002	0.003	0.001	0.001	0.002	0.001	0.003	0.002	0.01	0.00	0.009	0.001	0.001	0.001	0.003	0.001	0.011	n.d.
Ca	0.000	0.000	0.012	0.010	0.035	0.032	0.059	0.018	0.121	0.007	0.232	0.015	0.41	0.02	0.536	0.008	0.798	0.014	0.985	0.009	0.933	n.d.
Al	1.034	0.014	1.036	0.009	0.999	0.011	1.074	0.020	1.133	0.014	1.242	0.011	1.43	0.03	1.516	0.015	1.809	0.010	1.969	0.013	1.889	n.d.
Si	2.966	0.011	2.961	0.009	2.947	0.027	2.922	0.020	2.861	0.013	2.756	0.011	2.57	0.02	2.471	0.014	2.191	0.010	2.022	0.013	2.091	n.d.
Mg	0.000	0.000	0.000	0.001	0.000	0.000	0.000	0.000	0.000	0.000	0.000	0.000	0.00	0.00	0.001	0.000	0.000	0.000	0.001	0.000	0.008	n.d.
Ti	0.001	0.002	0.001	0.001	0.006	0.012	0.003	0.001	0.003	0.002	0.001	0.001	0.00	0.00	0.002	0.002	0.000	0.001	0.000	0.000	0.000	n.d.
Ba	0.000	0.000	0.013	0.004	0.020	0.037	0.000	0.000	0.001	0.002	0.001	0.001	0.00	0.00	0.000	0.000	0.000	0.000	0.000	0.000	0.000	n.d.
Mn	0.000	0.001	0.000	0.001	0.020	0.022	0.001	0.002	0.001	0.001	0.000	0.000	0.00	0.00	0.000	0.000	0.001	0.001	0.000	0.000	0.000	n.d.
Sr	0.000	0.000	0.000	0.000	0.005	0.009	0.000	0.000	0.000	0.000	0.000	0.000	0.00	0.00	0.000	0.000	0.000	0.000	0.000	0.000	0.000	n.d.
$\Sigma$ cations	5.028	0.007	5.011	0.006	5.060	0.068	5.014	0.004	5.018	0.013	5.009	0.007	5.01	0.01	5.001	0.006	5.007	0.002	5.006	0.004	4.995	n.d.
$\Sigma$ T site	4.000	0.004	3.998	0.002	3.946	0.033	3.997	0.002	3.994	0.004	3.998	0.003	4.00	0.01	3.988	0.004	4.000	0.003	3.991	0.002	3.981	n.d.
$\Sigma$ M site	1.028	0.006	1.013	0.007	1.114	0.098	1.017	0.005	1.024	0.014	1.011	0.005	1.01	0.01	1.014	0.008	1.007	0.003	1.015	0.005	1.014	n.d.
Or %	97.36	1.20	79.12	7.74	42.95	6.41	0.32	0.07	2.20	0.51	1.30	1.21	2.30	0.53	2.57	0.54	0.08	0.02	0.10	0.00	0.77	n.d.
Ab	2.62	1.21	19.70	6.79	53.70	5.18	93.83	1.85	85.92	0.76	75.61	0.39	56.67	1.84	43.93	0.70	20.39	1.44	1.34	0.29	3.02	n.d.
An	0.02	0.02	1.18	1.03	3.35	3.02	5.86	1.79	11.88	0.67	23.10	1.55	41.03	2.08	53.50	0.88	79.53	1.43	98.87	0.65	96.22	n.d.



Band <i>n</i> **	Raman shifts (cm <sup>-1</sup> )																					
	Avg. ±σ 6	Avg. ±σ 8	Avg. ±σ 6	Avg. ±σ 4	Avg. ±σ 9	Avg. ±σ 2	Avg. ±σ 8	Avg. ±σ 8	Avg. ±σ 11	Avg. ±σ 1	Avg. ±σ 3											
I <sub>a</sub>	513.08	0.13	512.76	0.28	512.92	0.40	507.65	0.10	507.82	0.28	510.65	0.92	510.41	0.90	509.30	0.21	504.90	0.41	504.80	n.d.	505.13	1.15
I <sub>b</sub>	475.85	0.32	476.99	0.66	474.75	0.30	479.73	0.15	479.24	0.23	479.80	0.21	480.58	0.65	479.88	0.43	484.60	0.35	487.60	n.d.	484.42	1.03
I <sub>c</sub>	454.13	0.23	454.86	1.16	456.65	0.58	457.80	0.14	457.80	0.94	455.19	1.63	455.70	2.53	443.25	1.64	460.56	2.11	461.96	n.d.	471.45	2.35
II <sub>max</sub>	285.32	0.28	282.11	0.38	284.70	0.25	290.73	0.22	290.47	0.15	284.65	0.21	286.49	1.63	285.44	1.31	285.60	0.38	285.40	n.d.	267.49	1.02
III <sub>max</sub>	157.12	0.67	156.51	1.12	160.33	4.18	185.85	0.10	184.76	0.64	161.10	1.13	177.58	1.12	178.64	1.52	196.60	3.09	198.60	n.d.	183.48	n.d.

\* Number of EMP sample spots analyzed. Averages are shown for multiple microprobe samplings locations. \*\* Number of Raman samples analyzed. Samples: 67513; lunar sample collection (U.S. government) as described Jolliff & Haskin (1995). We thank Monica Grady and the Natural History Museum of London for providing samples of NWA773. We are grateful to Marvin Kilgore for making portions of this meteorite available to the scientific community for study. The sample was fully described by Jolliff *et al.* (2003). n.d.: no data determined.

rock mixtures. The peak positions in Tables 2 and 3 are the averaged values obtained from multiple spots of each sample. The relatively large standard deviations in the Raman shift of the band maximum in Group III (150–190 cm<sup>-1</sup>) occur because this band lies close to the cutoff edge of the optical filter used to minimize the Rayleigh-scattered laser light from reaching the CCD camera. This filter yields a large curving background at low Raman shift frequencies (<180 cm<sup>-1</sup>), which in turn introduces uncertainties in determining peak positions.

Numerous studies, including both experimental observations and theoretical calculations, have been published over the past 30 years on the Raman and infrared spectral peak assignments of feldspar-group minerals. For all of these feldspar minerals, however, the observed number of Raman peaks is usually much lower than that predicted by group theory (von Stengel 1977, Dowty 1987, McMillan *et al.* 1982, and references therein, Sharma *et al.* 1983, Matson *et al.* 1986, McKeown 2005). Causes for the discrepancies between predicted and actual number of Raman peaks include: (a) much smaller pseudo-unit-cell in the triclinic structure, which determines the actual number of vibrational modes, (b) accidental degeneracies between the vibrational modes, and (c) the inability to detect weak peaks in the spectra above background noise (White 1974, Sharma *et al.* 1983). The results of group analyses and force-field calculations, plus other types of vibrational studies, have progressively developed into a general agreement on vibrational band assignments in feldspar-group minerals. The assignments [based on McKeown's (2005) calculations for low albite] show that the two strongest Raman bands in the 450–520 cm<sup>-1</sup> spectral region (Group I) belong to the ring-breathing modes of the four-membered rings of tetrahedra. The Raman peaks in Groups II and III (below 400 cm<sup>-1</sup>) correspond to rotation–translation modes of the four-membered rings and cage-shear modes, respectively. The weaker Raman peaks in the 900–1200 cm<sup>-1</sup> region (Group V) were assigned to the vibrational stretching modes of the tetrahedra. The mid- to weak-strength peaks in the 700–900 cm<sup>-1</sup> region (Group IV) belong to the deformation modes of the tetrahedra.

#### Raman spectra of the end members

Typical Raman spectra for the low-temperature end-member feldspars (maximum microcline, low albite, and anorthite-*P*), are presented in Figure 3. The distinct position of the peaks and the low sample-to-sample variability (<0.2 cm<sup>-1</sup>) of the I<sub>a</sub> peak position offer the first-order criterion for distinguishing the compositional end-members, *i.e.*, 513.3 cm<sup>-1</sup> for maximum microcline, 507.6 cm<sup>-1</sup> for low albite, and 504.6 cm<sup>-1</sup> for anorthite-*P*. All three end-members exhibit a triplet of peaks in Group I, although the intensity of peak I<sub>c</sub>

at  $461.9\text{ cm}^{-1}$  in anorthite-*P* is very weak compared to the intensity of the same peak in the Raman spectra of the other two end-members ( $I_c$  occurs at  $453.9\text{ cm}^{-1}$  for

maximum microcline and  $456.6\text{ cm}^{-1}$  for low albite). The motion of the oxygen atoms in the breathing mode of the four-membered ring is perpendicular to the  $T-T$

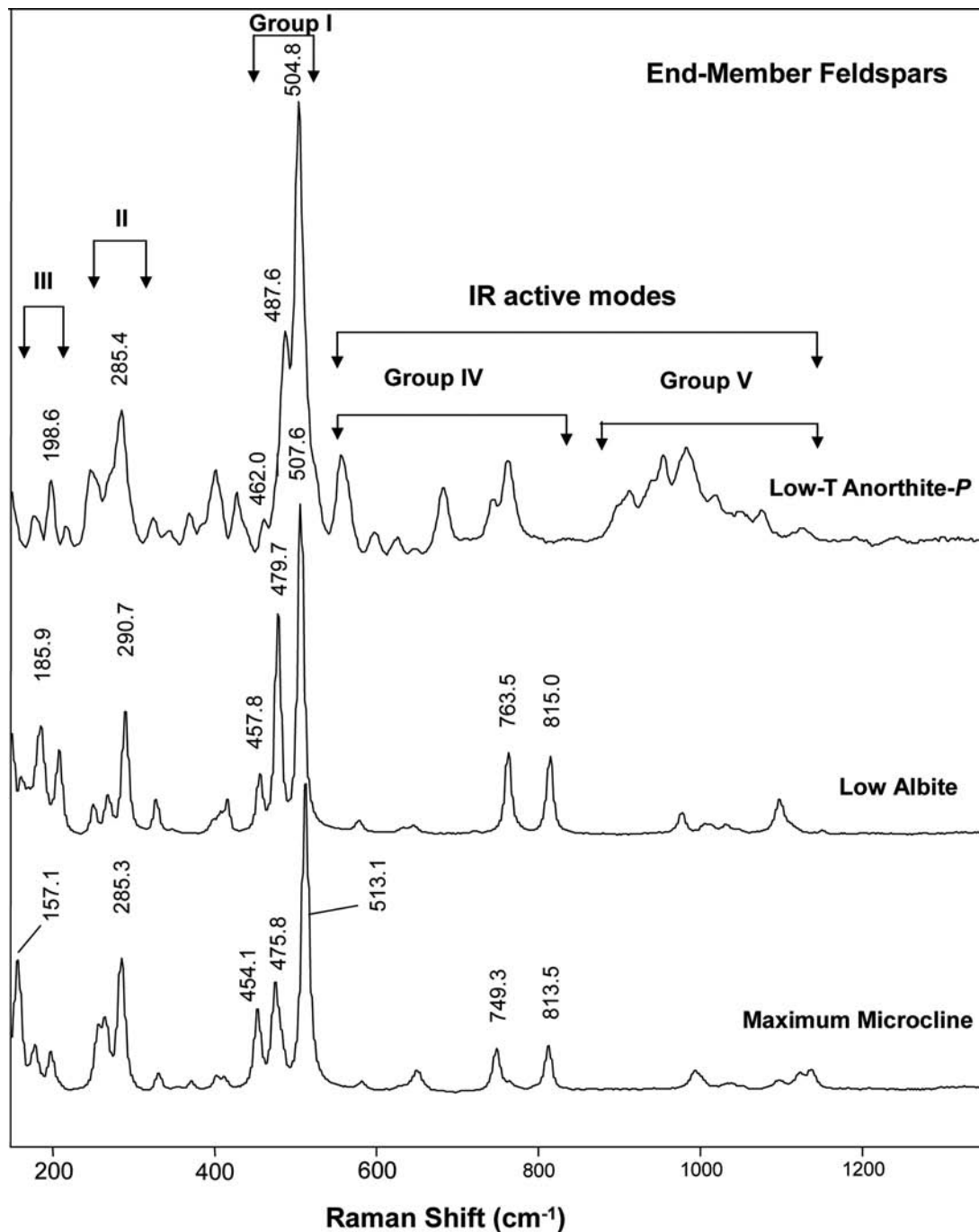


FIG. 3. Raman spectra of the compositional end-members maximum microcline, low albite, and low-temperature anorthite.

TABLE 3. RAMAN CHARACTERIZATION OF INDIVIDUAL FELDSPAR PHASES IN THE FIELD SAMPLES ORDERED ACCORDING TO THE PROPORTION OF Or, Ab AND An

Field sample label	Feldspar phase	Powder XRD label	EMP feldspar distribution				Raman band frequency (cm <sup>-1</sup> )					Raman SpecID search results				
			Or	Ab	An	n*	I <sub>a</sub>	I <sub>b</sub>	I <sub>c</sub>	II <sub>max</sub>	III <sub>max</sub>	n**	1 <sup>st</sup> hit	2 <sup>nd</sup> hit	3 <sup>rd</sup> hit	misses
EPSc #1	Microcline		96.68	3.26	0.06	6	512.9	475.8	453.6	285.2	157.6	6	6	0	0	0
EPSc #313	Microcline		97.36	2.62	0.02	8	513.1	475.9	454.1	285.3	157.1	6	6	0	0	0
EPSc 313-4	Microcline	MM,IM	96.50	3.50	0.01	6	512.9	475.6	454.1	285.0	157.2	4	4	0	0	0
JDP 109940	Microcline		94.60	5.40	0.00	7	512.9	476.1	453.9	283.3	158.8	1	1	0	0	0
ASU BUR3460A	Microcline		93.81	6.19	0.00	9	512.8	475.6	454.2	285.6	156.2	12	7	4	1	0
JDP 109940	Orthoclase		96.85	3.14	0.01	2	513.1	475.4	454.0	283.0	152.1	3	3	0	0	0
EPSc#313-10	Orthoclase	OR	90.95	8.86	0.20	4	513.3	475.0	453.1	280.5	153.0	4	4	0	0	0
ASU H314	Orthoclase		75.75	22.88	1.37	8	512.7	477.1	454.8	282.3	156.2	8	8	0	0	0
ASU H314.4b	Sanidine		85.78	13.75	0.47	1	511.9	477.9	454.5	283.7	154.0	1	1	0	0	0
EPSc#27-32	Sanidine	SA	61.05	37.16	1.76	3	514.2	473.7	457.3	284.5	158.6	4	3	1	0	0
LC002-14088	Sanidine		97.04	2.93	0.03	2	512.8	476.4	454.2	281.0	156.3	1	1	0	0	0
Tablet in welded pumice	Sanidine		42.95	53.70	3.35	6	512.9	474.8	456.7	284.7	160.3	6	6	0	0	0
Tablet in non-welded pumice	Sanidine		41.38	57.16	1.46	8	513.3	474.6	455.7	284.5	164.3	7	7	0	0	0
465(2,B)	Sanidine		30.02	66.61	3.37	8	513.0	473.5	463.6	284.2	165.1	5	5	0	0	0
164	Sanidine		26.71	69.08	4.22	5	512.6	475.8	458.9	284.5	156.4	5	6	0	0	0
465(1,A)	Sanidine		27.00	68.97	4.04	9	513.1	473.8	459.2	284.2	164.0	7	7	0	0	0
Albite	Albite		0.0	100.00	0.00	0	507.6	479.4	457.0	290.9	186.0	1	1	0	0	0
ASU BUR3460A	Albite		0.48	99.39	0.13	3	507.7	479.3	458.3	291.0	185.6	3	3	0	0	0
JDP 109940	Albite	HA	0.57	98.82	0.61	3	507.6	479.3	461.2	290.1	184.1	3	1	2	0	0
EPSc#313-4	Albite		0.76	98.40	0.90	2	507.7	479.1	455.9	289.7	185.3	2	2	0	0	0
EPSc#313-10	Albite	LA	1.34	97.91	0.75	2	507.9	479.4	457.3	291.0	186.4	1	1	0	0	0
#162	Albite		0.35	93.66	5.99	4	507.7	479.7	457.8	290.7	185.9	4	4	0	0	0
JDP # 10-997	Peristerite		2.20	85.92	11.88	10	507.8	479.2	457.8	290.5	184.8	6	6	0	0	0
ASU 314.4b	Oligoclase		1.30	75.60	23.10	4	510.7	479.8	455.2	284.7	161.1	3	3	0	0	0
Grey anorthosite	Andesine		0.76	66.33	32.91	8	509.8	480.3	460.6	285.3	176.8	8	8	0	0	0
LC002-14088	Andesine		2.30	56.67	41.03	12	510.4	480.6	455.7	286.5	177.6	6	6	0	0	0
#3-8	Andesine		5.47	55.24	36.29	7	510.3	480.6	449.2	285.6	176.9	8	8	0	0	0
#C-3	Andesine		0.32	53.70	46.05	6	509.3	481.2	445.7	286.6	174.9	6	6	0	0	0
#3-14	Andesine		3.37	49.02	47.61	6	510.3	480.8	447.8	286.0	176.9	6	6	0	0	0
ASU WAR4524	Labradorite		1.34	46.06	52.60	9	509.2	481.7	451.7	285.9	179.6	8	8	0	0	0
AU BUR3080A	Labradorite		3.23	45.65	57.12		509.5	481.5	463.8	286.2	189.0	9	9	0	0	0
PG721	Labradorite AN		2.57	43.93	53.50	7	509.3	479.9	443.3	285.4	178.6	9	8	1	0	0
85-5-20	Labradorite		3.14	40.16	56.70	6	508.8	480.5	447.0	286.1	180.4	6	6	0	0	0
LSJ 80-192	Labradorite		1.35	36.52	62.13	8	508.9	480.5	444.0	285.9	183.3	11	11	0	0	0
ASU WAR4524(1)	Bytownite		0.25	24.03	75.72	1	504.9	484.6	460.6	285.6	196.6	1	1	0	0	0
OGG-138B	Bytownite		0.08	20.39	79.53	9	504.9	484.6	460.6	285.6	196.6	22	20	2	0	0
#67512,7075	Low anorthite		0.10	1.86	98.04	Ti	504.8	487.6	462.0	285.4	198.6	3	3	0	0	0
NWA 773	Shocked anorthite		2.00	10.00	88.00	Til	505.1	484.4	471.4	n.d.	n.d.	1	1	0	0	0
Mt. Erebus	Ternary fsp		15.88	68.85	15.27	10	511.0	476.0	n.d.	283.2	162.7	7	n.a. <sup>‡</sup>	n.a.	n.a.	n.a.
EPSc#27-32	Oligoclase		6.75	65.53	27.72	5	507.8	479.2	n.d.	n.d.	n.d.	2	n.a.	n.a.	n.a.	n.a.
ASU WAR0579	Ternary fsp		25.92	64.87	9.21	4	510.2	478.8	457.5	287.5	160.2	11	n.a.	n.a.	n.a.	n.a.
ASU WAR0579	Ternary fsp		33.95	56.93	9.12	4	511.1	477.8	454.6	286.2	156.5	11	n.a.	n.a.	n.a.	n.a.

Ti: Table I, Jolliff & Haskin (1995). Til: Table II, Jolliff *et al.* (2003). <sup>‡</sup> Unable to distinguish high-temperature ternary feldspars from high-temperature plagioclases. Symbols: MM: maximum (ordered) microcline, IM: intermediate microcline, OR: orthoclase, SA: sanidine, LA: low (ordered) albite, HA: high (disordered) albite, AN: anorthite, fsp: feldspar, n\*: number of samples characterized by electron-microprobe analysis, n\*\*: number of Raman scans, n.d.: no data, n.a.: not applicable.

line, making variations in the  $T-O-T$  bond angles a factor in determining the position of the Group-I Raman peaks. The Si–O–Al bond angles are clearly distributed in two clusters (Fig. 4c), which may explain the strong doublet aspect of the spectral pattern ( $I_a$  and  $I_b$ , with

extremely weak  $I_c$ ) in the Group-I region of anorthite. In comparison, the Si–O–Si and Si–O–Al bond angles in maximum microcline and low albite are distributed in roughly three groups (Figs. 4a, b). This distribution

of bond angles explains the triplet spectral pattern in the Group-I region of these two end members.

The spectra of the three end-member feldspars exhibit similar patterns, but most bands in the spectrum of anorthite-*P* are shifted toward lower frequencies. The bands of anorthite-*P* in the spectral regions of Groups I, II, and IV are also less well resolved owing to the broader band-widths.

Group-V bands (Fig. 3) are associated with breathing modes of tetrahedra involving *T*-O stretching vibrations. The number of component peaks in the Group-V spectral region (900–1200  $\text{cm}^{-1}$ ) clearly reflects the Si:Al variations induced by varying proportions of Ca, Na and K in the structures. Low albite has six well-resolved peaks and two shoulders in this region; maximum microcline has seven well-resolved peaks and one shoulder, and anorthite-*P* has seven well-resolved peak and three shoulders (Fig. 3).

The spectral patterns of low albite and maximum microcline are similar in the Group-IV region, reflecting the similarity in their crystallographic structure with regard to the degree of Al-Si order. Their Group-IV Raman spectral patterns are characterized by a pair of moderately strong, sharp peaks at 764 and 815  $\text{cm}^{-1}$  for low albite, and 749 and 814  $\text{cm}^{-1}$  for maximum microcline. The spectral pattern of anorthite-*P* in the Group-IV region differs in that all the bands are shifted to lower frequencies and have different rela-

tive intensities. The difference in the pattern of the anorthite-*P* bands is due to the higher Al:Si ratio and is consistent with increased contributions of the Al-O and Al-O-Si bonds to the vibrations in the Group-IV region (McMillan *et al.* 1982, von Stengel 1977). The uniqueness of these Group-IV and Group-V patterns in the end-member feldspars allows the low albite and maximum microcline to be distinguished from each other and from anorthite-*P*.

#### *K-feldspar samples with different degrees of Si-Al order*

As a series, the three structural types of potassium feldspar, microcline, orthoclase, and sanidine, display increasing structural disorder in the distribution of the one Al and three Si cations within the rings of four linked tetrahedra of the feldspar lattice. Maximum microcline has the highest degree of Si-Al order, with the Al cation occurring at a unique tetrahedral site, whereas the Si cations occur in the remaining tetrahedral sites (Fig. 2, Smith & Brown 1988). In orthoclase, the two unique sites are occupied by two Si cations, but the Al and third Si cation are randomly distributed between the remaining sites. High sanidine has the highest degree of Si-Al disorder, where all three Si

TABLE 4. A COMPARISON OF THE RAMAN FREQUENCIES OF THE VARIOUS FELDSPARS

MM	OR	SA	LA	HA	Pl	An-I	An-P
1138	1136 sh	...	1152	1139	1316	...	1194
1124	1123	1120	1113 sh	1106 sh	...	1110 sh	1126
1097	1198 sh	1094 sh	1099	1098	1086 sh	...	1077
...	...	...	1046	...	...	...	...
1036	1036 sh	1030 sh	1033	1030	1032 sh	1016	1020
...	...	...	1013	...	...	...	...
...	...	...	1008	...	...	...	...
994	988	1001	978	977	987	978	984
...	...	...	...	...	...	959 sh	956
...	...	...	...	...	915 sh	913	914
813	810	804	815	812	797	791	795 sh
749	748	776	764	762	767	764	764
...	...	726 sh	721	737 sh	742 sh	743	745
651	(655) <sup>1</sup>	(644)	646	651	652	680	683
629 sh <sup>2</sup>	(625) <sup>1</sup>	...	634	636	636 sh	626	626
583	583	571	580	578	569	564	557
513	513	514	507	507	510	505	504
476	475	475	479	476	482	484	488
454	454	454 sh	457	452	(453) <sup>1</sup> sh	425	429
...	...	...	416	...	...	...	...
403	406	405	408	406 sh	410	405	402
...	...	...	400	399	397 sh	...	...
372	370	368	349	346	...	367	371
332	330	...	329	327	336	322	325
286	282	285	291	287	288	285	285
266	265	...	269	266 sh	...	...	272 sh
258	255 sh	...	252	254	...	248	248
200	197	197	209	206	202 sh	197	199
178	176	...	186	182	177	183	178
158	155	165	140	156	...	148	149

Symbols: MM: maximum microcline, OR: orthoclase, SA: sanidine, LA: low albite, HA: high albite, Pl: plagioclase ( $\text{An}_{50}$ ), An-I: high-T anorthite-I, An-P: low-T anorthite-P. <sup>1</sup> Peak positions in parentheses were derived by peak deconvolution. <sup>2</sup> sh: unresolved shoulder.

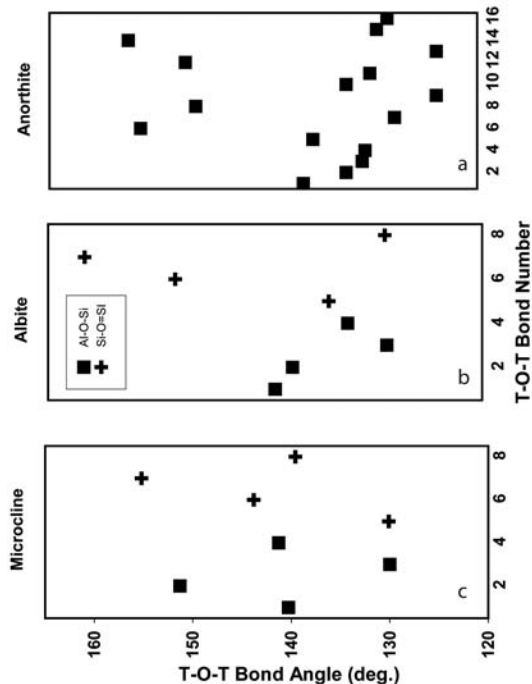


FIG. 4. Distribution of *T*-O-*T* (*T*: Si, Al) bond angles among the feldspar end-members versus bond-angle assignment number.

cations and one Al cation are randomly distributed among all four tetrahedral sites.

The Raman spectra of the three potassium-rich alkali feldspar structures are compared in Figure 5. It is readily apparent that the position of the strongest Raman band,  $I_a$ , is similar in all samples, ranging only  $0.4\text{ cm}^{-1}$  from  $512.7$  to  $513.1\text{ cm}^{-1}$ . The widths of all Raman peaks in the  $\text{KAlSi}_3\text{O}_8$  structures increase with increasing Si–Al disorder. The well-resolved Group-I triplet widens to a less well-resolved triplet in the orthoclase spectrum, and to a doublet in the spectrum of sanidine. The Raman spectra for each of these three potassium-rich feldspar phases are reproducible, and a comparison of the band shapes in the Raman spectra allow them to be

distinguished from each other and from other feldspar structural types.

#### *Sanidine with K–Na substitution*

There is an additional compositional disorder in the alkali feldspars where  $\text{Na}^+$  substitutes for  $\text{K}^+$ . The Raman spectrum of sanidine shown in Figure 5 is representative of all eight samples of disordered alkali-feldspar in which the albite content ranges from  $\text{Ab}_{14}$  to  $\text{Ab}_{73}$ . Because the interactions between the extra-framework cations in the framework oxygen atoms in feldspars are weaker than the  $M\text{--O}$  interactions in other minerals such as olivine and pyroxene,

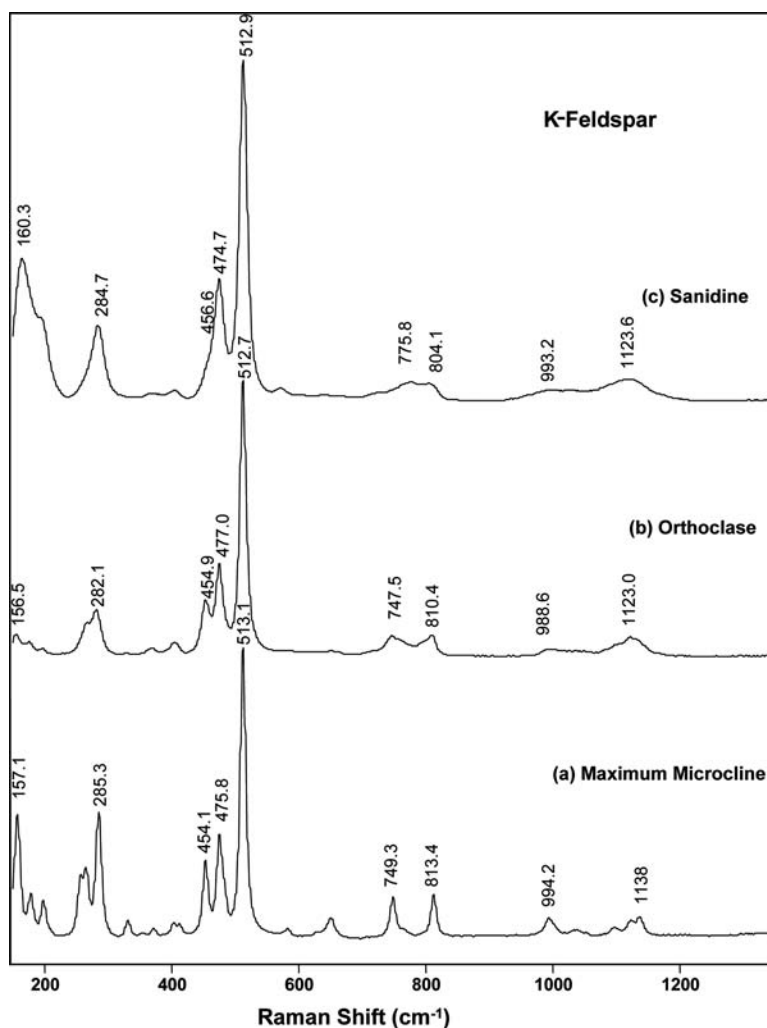


Fig. 5. Raman spectra of the K-feldspars with different degrees of Al–Si order: maximum microcline, orthoclase, and sanidine.



the Raman spectra of the feldspars are not sensitive to Na and K content and do not differ significantly over the compositional range studied.

*Sodium-rich feldspars with different degrees of Si–Al order*

Of the twenty-one spectra acquired for Na-rich alkali feldspar samples, only two unique Raman spectra were obtained; 19 sample points have Raman spectra consistent with low albite or low albite in peristerite

(Figs. 6a, b), and two sample points yielded Raman spectra like that of disordered, high albite (Fig. 6c). The strongest Raman band,  $I_a$ , for low albite consistently occurs at  $507.6\text{ cm}^{-1}$ , which is  $5\text{ cm}^{-1}$  lower than from the band position of the potassium feldspars. Thus, sanidine and ternary feldspars with considerable Na content have higher  $I_a$  Raman peak positions than that of low albite.

The Raman spectrum for high albite (Fig. 6c) shows broader Raman peaks than low albite. The width of the Group- $I_a$  band is  $\sim 13.7\text{ cm}^{-1}$  in high albite compared

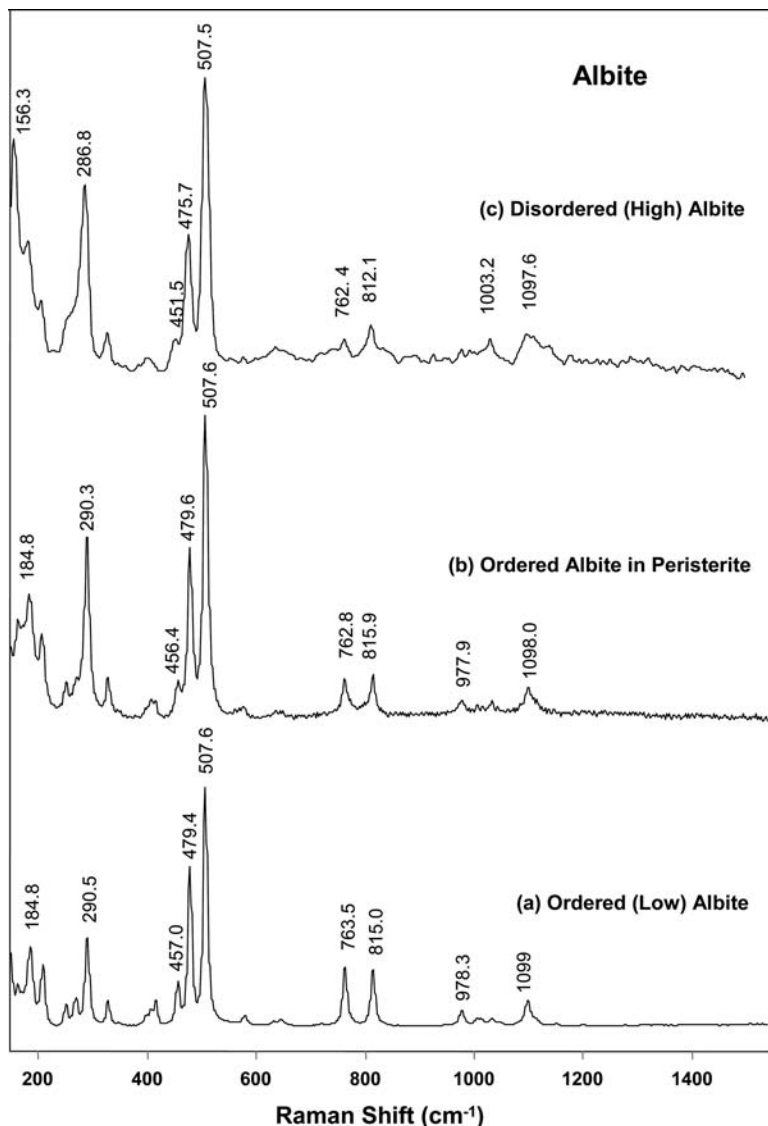


FIG. 6. Raman spectra of Na-feldspars with different degrees of Al–Si order: low-temperature albite, peristerite, and high-temperature albite.

with  $8.4\text{ cm}^{-1}$  in low albite. Band broadening introduces a loss of spectral resolution in the major and minor peaks of high albite, a trend observed in the Raman spectra of any of the feldspar structures with increased Al–Si disorder. The spectrum of high albite (Fig. 6c) is consistent with that first published by Farmer (1974) and later explored in detail by McKeown (2005). All major Raman bands of high albite, except the  $I_a$  Raman band at  $507.5\text{ cm}^{-1}$ , also show a slight downshift in peak positions compared to the corresponding peaks of low albite. Other than band broadening and slight shift in the band of high albite, the Raman spectra of high albite and low albite found in this study are quite similar, consistent with the fact that they both have a triclinic structure (Smith & Brown 1988). The fact that the  $I_c$  Raman band at  $451.5\text{ cm}^{-1}$  is still resolved in our high albite Raman spectrum would, by comparison of our spectrum with the spectra shown by McKeown (2005, Fig. 6), indicate that our particular samples probably had not been heated much beyond  $500^\circ\text{C}$ . This indication is consistent with the triclinic, high albite classification (Ribbe 1983b).

Peristerite is a feldspar intergrowth formed at elevated annealing temperatures, and consists of optically unresolved lamellae of low albite ( $An_{<10}$ ) and oligoclase ( $An_{10-30}$ ) whose Raman spectrum is that of the predominant low albite host. Thus the Raman spectra of low albite (Fig. 6a) and peristerite (Fig. 6b) are nearly identical both in peak positions and band widths. There is no evidence in the Raman spectrum of our peristerite sample for the presence of the exsolved oligoclase.

### *The calcium-rich feldspars*

Three structurally significant and distinct anorthite samples were included in this study: low-temperature anorthite with a primitive unit cell (anorthite-*P*), high-temperature anorthite with a body-centered unit cell (anorthite-*I*), and a meteoritic, pressure-shocked lunar anorthite. Representative Raman spectra of these three varieties of anorthite are shown in Figure 7. These spectra are consistent with previously published Raman spectra for anorthite (Daniel *et al.* 1995b, 1997, Gillet *et al.* 1977, Matson *et al.* 1986, McMillan *et al.* 1982, Sharma *et al.* 1983). All three spectra have their strongest Raman band ( $I_a$ ) between  $504.8$  to  $505.1\text{ cm}^{-1}$ . The well-resolved  $I_b$  Raman band occurs between  $484$  and  $488\text{ cm}^{-1}$ , but the third band, ( $I_c$  at  $461.2\text{ cm}^{-1}$ ) of the Group-I triplet is very weak in the anorthite-*P* spectrum and is not resolved at all in the Raman spectra of anorthite-*I* and shocked anorthite. Because of the overlap of the three Group-I Raman bands in anorthite, the exact positions of the peaks are best determined by peak deconvolution (see Table 3).

The Raman spectrum of anorthite-*I* (Fig. 7b) is taken from a plagioclase sample exhibiting classic Huttenlocher intergrowths and an An content consistent

with bytownite ( $An_{70-90}$ ). The two exsolved feldspar phases in exsolution lamellae, anorthite-*I* and labradorite ( $An_{50-70}$ ), cannot be resolved with the optical microscope used with the Raman microprobe, nor were they resolved with the broad ( $10\text{ }\mu\text{m}$ ) beam of the EMP. The resultant Raman spectrum (Fig. 7b) is dominated by the spectral features of the major component, high-temperature anorthite-*I* ( $An_{100}$ , Mernagh 1991). A more detailed discussion of the differences between the bytownite structure and the anorthite structure can be found in Ribbe (1983a).

The spectrum of the shocked anorthite ( $An_{96}$ , Fig. 7c), obtained from the core of a plagioclase grain in the lunar meteorite NWA 773, shows much broader band-widths and a loss of spectral resolution expected in the Raman spectrum of a distorted, vitrified structure. This spectrum is similar to the room-temperature Raman spectrum of an anorthite sample decompressed from a maximum pressure of  $15.8\text{ GPa}$  (Daniel *et al.* 1997). Daniel *et al.* (1995a) attributed the appearance of a broad, medium-intensity band around  $1000\text{ cm}^{-1}$  in the Raman spectrum of shocked anorthite (Fig. 7c) to the pressure-induced formation of aluminosilicate glass within the feldspar structure. This broad band occurs in the Raman spectrum where the Si–O<sub>nb</sub> (O<sub>nb</sub>: non-bridging atom of oxygen) stretching vibrational modes of less polymerized silicates would normally occur. Whereas little change is observed in the  $I_a$  peak positions if Al–Si disorder increases in K- and Na-feldspars, the  $I_a$  peak position shifts upward with an increase of disorder in the calcium feldspars:  $504.4\text{ cm}^{-1}$  for anorthite-*P*,  $506.5\text{ cm}^{-1}$  for our shocked anorthite sample, and  $\sim 508\text{ cm}^{-1}$  for a glass of  $\text{CaAl}_2\text{Si}_2\text{O}_8$  composition quenched from  $1575^\circ\text{C}$  in air (Sharma *et al.* 1983). The positions and relative intensities of the major Raman peaks of the shocked anorthite suggest that it is partially converted to maskelynite (Wang *et al.* 1999, 2004b).

### *High-temperature plagioclase*

Our study included twelve samples of three intermediate plagioclase compositions: one oligoclase sample ( $An_{24.4}$ ), five andesine samples ( $An_{33.6-46.3}$ ), and six labradorite samples ( $An_{51.5-63.5}$ ). Two mineral samples with bytownite compositions ( $An_{75}$  and  $An_{80}$ ) are included in the discussion of the anorthite samples because their Raman spectra are consistent with high-temperature anorthite-*I*, and their structures differ from the three samples of calcic plagioclase listed here. One labradorite sample (PG721,  $An_{56.1}$ ) exhibits a Bøggild submicrometric intergrowth. As with the other submicrometric intergrowths studied here, individual phases in the Bøggild lamellae cannot be analyzed separately. The resultant spectra of the Bøggild lamellae represent overlapping bands of the spectra from two individual phases and are indistinguishable from the Raman spectra of other labradorite samples.

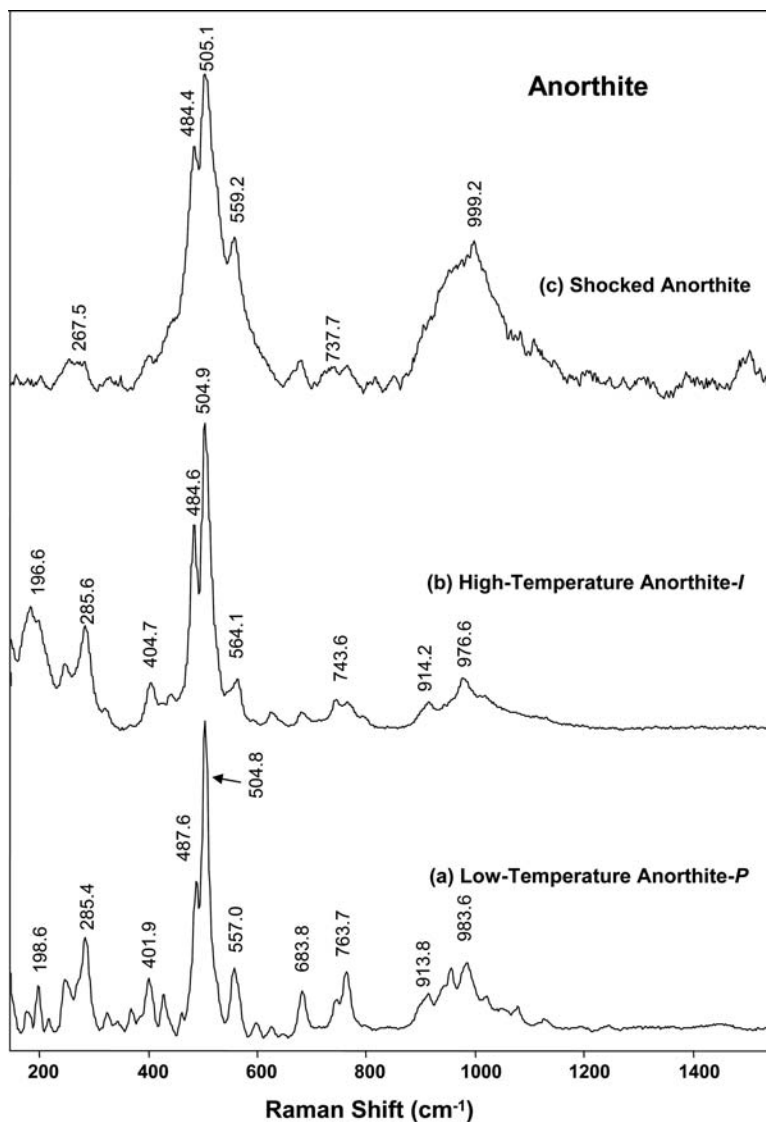


FIG. 7. Raman spectra of Ca-feldspars: anorthite-*P*, anorthite-*I*, and pressure-temperature-shocked anorthite.

Raman spectra representing these three compositionally distinct groups of plagioclase are shown in Figure 8. They all have similar Raman spectral patterns. More importantly, these mid-An plagioclase samples have distinct  $I_a$  peak positions ranging from 509.1 to 510.7  $\text{cm}^{-1}$  that are not midway between the Raman peaks of the crystalline end-members low albite and anorthite-*P*. They occur at higher frequencies than either end-member. These plagioclase samples also have a fairly prominent  $I_b$  band near 480  $\text{cm}^{-1}$ . The separation of the  $I_a$  and  $I_b$  bands (average  $\sim 30 \text{ cm}^{-1}$ ) in the spectra

of these samples is closer to that of a Na-feldspar (average  $\sim 30.4 \text{ cm}^{-1}$ ) than a Ca-feldspar (average  $\sim 19.5 \text{ cm}^{-1}$ , Fig. 8). The  $I_c$  band is seen only as a shoulder in the spectrum of oligoclase ( $\text{An}_{23}$ ), but its presence in the spectra of andesine and labradorite can only be determined through the spectral deconvolution of the Group-I peaks (Table 3).

Although the  $I_a$  peak positions and  $I_a$ - $I_b$  peak separations make these mid-An plagioclase samples stand out as a distinct group, the differences among these twelve individual spectra are relatively minor. There is

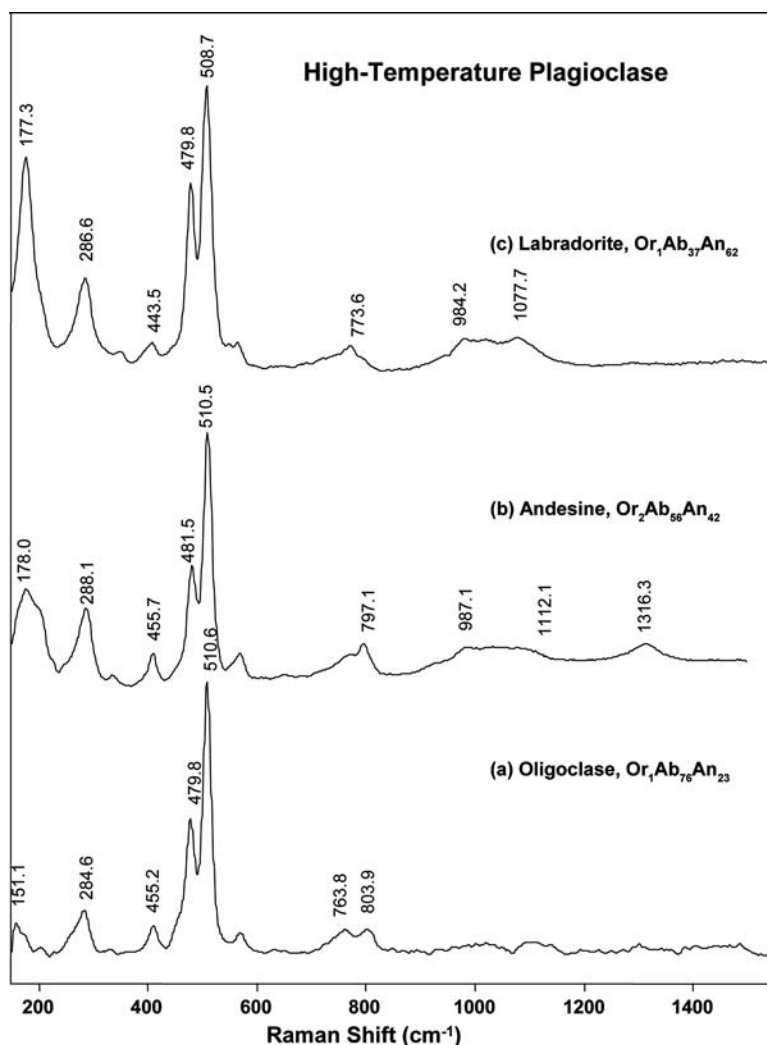


FIG. 8. Raman spectra of the plagioclases

no obvious correlation between An content and the  $I_a$  peak positions or the  $I_a$  and  $I_b$  peak separations. Therefore, detailed information about the An content of these samples of intermediate-An high-temperature plagioclase cannot be determined from their Raman peak positions. The  $I_a$  peak positions and the separation of the  $I_a$  and  $I_b$  bands in the Raman spectra of these intermediate-An plagioclases do, however, allow us to distinguish them from the plagioclase end-members (albite and anorthite) as well as from the alkali feldspars.

#### *Ternary feldspars*

Four feldspar samples have elemental compositions high in  $\text{Na}^+$  with non-trivial amounts of both  $\text{K}^+$  and  $\text{Ca}^{2+}$  in the range of  $\text{Ab}_{\leq 84}\text{An}_{\geq 7}\text{Or}_{\geq 7}$ , a range normally associated with high-temperature ternary feldspars. This composition falls in the phase diagram for ternary feldspars (Fig. 1), between high-temperature (K, Na) sanidine and the high-temperature (Na, Ca) plagioclase. (In Fig. 1, we have overlain the isothermal lines separating the single-phase ternary compositional zone

from the two-phase compositional zone). The elemental compositions of the four ternary feldspar samples place them between the 750° and 900°C isotherms, and these compositions are consistent with the high-temperature origins of the samples, *e.g.*, a trachyte inclusion in a volcanic glass. The Raman spectral parameters of these samples of ternary feldspars (Fig. 9) do not match exactly the Raman spectra of any known feldspars discussed up to this point. They do, however, show the broad Raman bands normally associated with high-temperature, structurally disordered feldspars such as

sanidine or the high-temperature plagioclases. The  $I_a$  peak positions of three of the four ternary feldspar samples fall between 509 and 511  $\text{cm}^{-1}$ , similar to high-temperature plagioclase. The  $I_a$  and  $I_b$  band separations of these ternary feldspars (average 33  $\text{cm}^{-1}$ ) are larger than that of a Na-feldspar (average 30  $\text{cm}^{-1}$ ), but less than that of a K-feldspar (average 35  $\text{cm}^{-1}$ ). Although the variation in  $I_a$  peak positions is minor among these four ternary feldspar samples (Fig. 9), the variations in the  $I_b$  and  $II_{\text{max}}$  peak positions are relatively larger, which may reflect changes in composition. It is worth

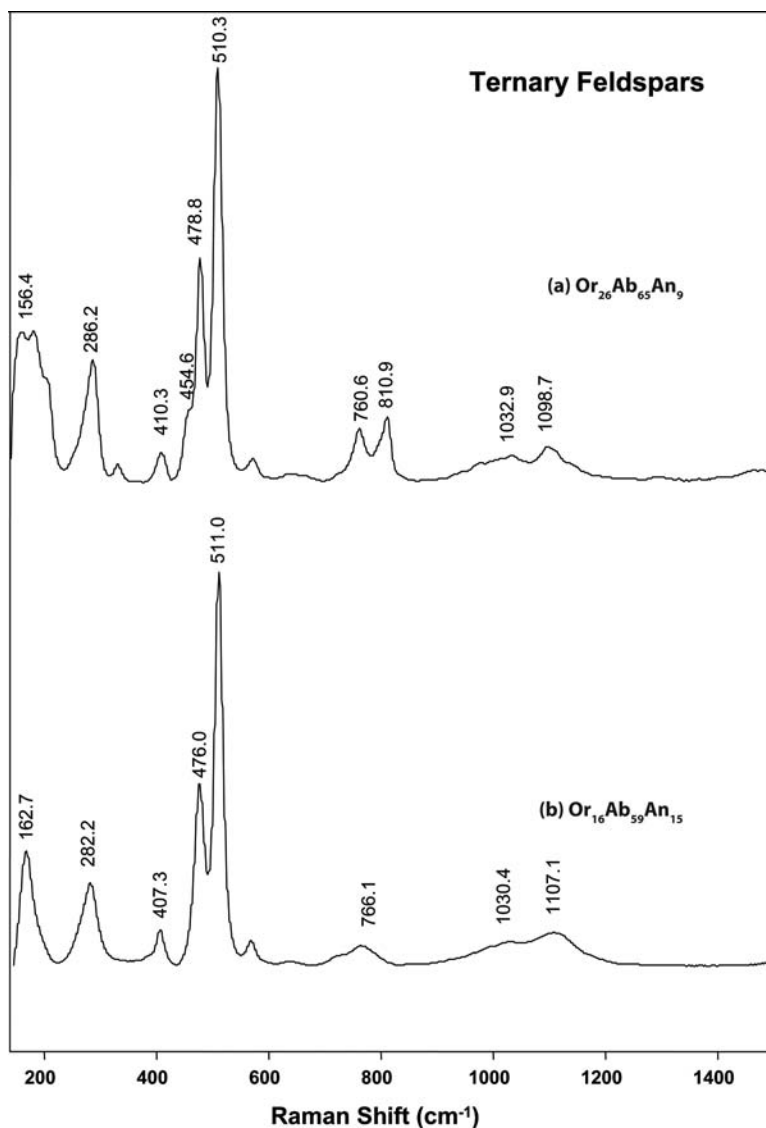


FIG. 9. Raman spectra of ternary (K-Na-Ca) feldspars.



noting that the ternary feldspar with low An content (Fig. 9a) still has a triplet band pattern in the Group-I region, which can be used as a criterion to distinguish it from the high-temperature plagioclases. These plagioclase samples have a similar position of the  $I_a$  peak, slightly smaller  $I_a - I_b$  peak separations, and a doublet peak pattern in Group-I region.

#### CLASSIFYING FELDSPARS USING RAMAN SPECTRA

##### *Classification of a feldspar based on Raman peak positions*

In this section of the discussion, we focus on how the Raman peak positions of the different feldspars correlate with their cation composition. In these comparisons, we use the five Raman peak positions in Table 3 labeled as  $I_a$ ,  $I_b$ ,  $I_c$ ,  $II_{max}$  and  $III_{max}$ . With the exception of the last four ternary feldspar samples listed in Table 3, all other feldspar samples lie on either the Or–Ab or Ab–An join of the phase diagram. We therefore selected two compositional parameters to use as quantitative measures of the cation proportions: the Or content for samples lying on the Or–Ab join of the ternary diagram and the Ab content for samples lying on the Ab–An join, in mol. % (Fig. 1). These two single parameters, % Or and % Ab, plotted on one axis are appropriate for analyzing the Raman frequency characteristics of these feldspar phases. In the case of the four high-temperature, ternary

single-phase feldspars, we have arbitrarily selected the % An content of the sample when plotting the data.

In Figure 10, we see that there is a general correlation between the  $I_a$  peak positions and the interstitial cation in the feldspars. In the case of the  $I_a$  peak, its position shifts to lower frequency across the range from Or<sub>100</sub> to Ab<sub>100</sub> to An<sub>100</sub>. A similar trend exists for the  $I_b$  peak positions, except that the  $I_b$  peak positions shift to higher frequency as the composition varies from Or<sub>100</sub> through Ab<sub>100</sub> to An<sub>100</sub> (Fig. 11). Nevertheless, the peak positions in these two trends are clustered, and no reliable quantitative correlation between Raman peak positions and cation proportions can be extracted from the two trends shown in Figures 10 and 11.

If instead of looking for quantitative correlations in the data, however, we look for clusters of data points around certain feldspar classes, as we see in Figure 10 and less clearly in Figure 11, we find that there are four distinct clusters of data points associated with different types of feldspar structures. The data in Figure 10 suggest that the position of the Raman peak  $I_a$  can be used to distinguish the following four types of feldspar:

1. All alkali feldspars of composition Or<sub>100–25</sub> (i.e., microcline, orthoclase or sanidine) have a  $I_a$  Raman peak position of  $513 \pm 1 \text{ cm}^{-1}$  regardless of crystallinity.
2. All high-temperature plagioclases of intermediate composition ~Ab<sub>75–30</sub> (including the ternary feldspars

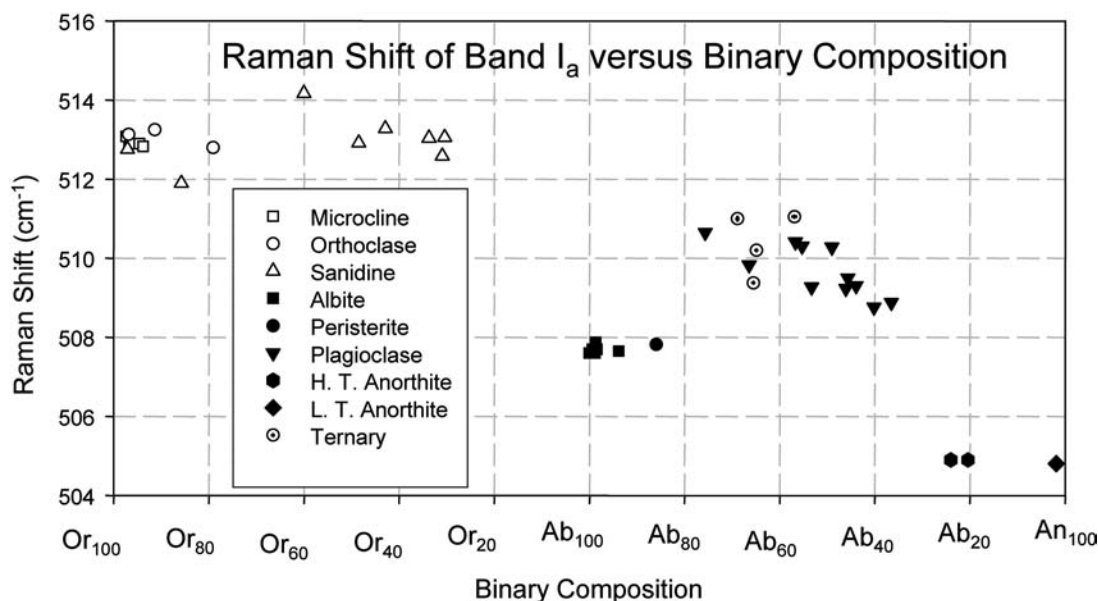


FIG. 10. Correlation between the Raman band  $I_a$  peak position and the feldspar binary composition along the Or–Ab and Ab–An joins.

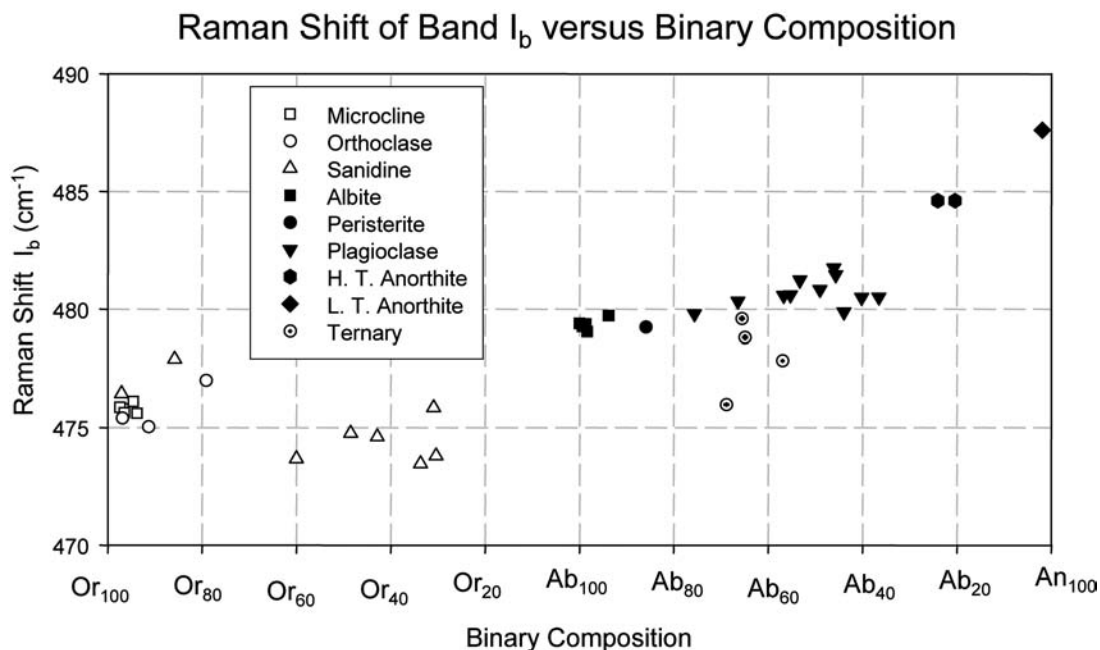


FIG. 11. Correlation between the Raman band  $I_b$  peak position and the feldspar binary composition along the Or–Ab and Ab–An joins.

studied), have a  $I_a$  Raman peak position of  $510 \pm 1 \text{ cm}^{-1}$ . (Because of the arbitrary way we defined the binary composition of the four true ternary feldspars, they also fall in this class).

3. All samples of low-temperature and high-temperature albite with  $\text{Ab}_{>85\%}$  exhibit a  $I_a$  Raman peak at  $507.7 \pm 0.1 \text{ cm}^{-1}$ .

4. All samples of anorthite ( $P$ ,  $I$  and shocked) with  $\text{An}_{>85\%}$  showing a  $I_a$  Raman peak of  $504.9 \pm 0.1 \text{ cm}^{-1}$ .

Similar correlations of the peak positions of the other four diagnostic Raman peaks ( $I_b$ ,  $I_c$ ,  $II_{\max}$  and  $III_{\max}$ ) versus the binary composition provide a similar, but less well resolved classification of feldspar types. The only exception to this general clustering of Raman peak positions occurs in the ternary feldspars. For these comparisons, we arbitrarily selected the % An content for the plots shown in Figures 10 and 11. The ternary feldspar data in these plots cluster with the Raman data of high-temperature plagioclase samples.

#### Full spectral pattern recognition and first derivative spectral search

Up to this point, we have shown that only four general feldspar structures (three of them being compositional end-members) can be identified on the basis of one or two peak positions in the Raman spectrum. The Raman spectra in Figures 5 through 9 show that struc-

tural variations of a given compositional end-member feldspar can be easily distinguished by considering the entire Raman spectral pattern, including peak positions, relative peak intensities, and band widths. This observation suggests that additional structural information can be extracted from the entire Raman spectrum using a spectral matching analysis. This process requires the selection of a standard set of Raman spectra samples with known structures and compositions and the application of a statistical search routine for comparing the Raman spectrum of an unknown feldspar with the spectra in the standard dataset. For the purpose of spectral identification, we use SPECTRAL ID (©1999–2000 Galactic Industries Corporation). The method of comparison we chose is based the first-derivative least-squares method. This correlation algorithm is similar to the Euclidian distance algorithm used to search the spectral database except that the unknown and library data are centered about their respective means before vector dot products are calculated. This particular correlation makes the Hit Quality Index (HQI) independent of spectral normalization. Furthermore, the use of the first derivative in the correlation algorithm reduces the effects of broad, nonlinear backgrounds, a problem commonly encountered in the Raman spectroscopy of fluorescing samples.

The initial database we developed includes typical Raman spectra of the following types of feldspars: (1)

maximum microcline, (2) orthoclase, (3) sanidine with  $\text{Or}_{85-90}$ , (4) low albite, (5) all three plagioclases, oligoclase, andesine and labradorite, (6) the high-temperature anorthite-*I*, and (7) the low-temperature anorthite-*P*. When we tested the initial database, it became apparent that we could not statistically differentiate between the Raman spectra of the three intermediate plagioclase compositions: oligoclase, andesine and labradorite. We therefore reduced our reference database to include only one typical plagioclase, labradorite. We also excluded the following varieties: (1) high albite (only two microscopic grains were available, precluding detailed analysis), (2) anorthoclase *s.s.* (we have no such sample of composition  $\text{Or}_{5-10}$  with  $\text{Ab}_{>90\%}$  and with negligible An), (3) shocked anorthite (only one lunar sample studied), and (4) the four ternary feldspar samples whose spectra do not appear to be unique. The characteristic spectral feature of the ternary feldspar is a  $\text{I}_a$  peak position at  $510\text{--}511\text{ cm}^{-1}$ , which is similar to the  $\text{I}_a$  peak of high-temperature plagioclase. There is too much variation in the weaker Raman bands of the ternary feldspars to designate a Raman spectrum as representative of all ternary feldspars.

Using the reduced database of the seven feldspar types noted above, the spectral matching routine SPECTRAL ID was applied to the ~200 individual Raman spectra generated during this study. The SPECTRAL ID options were set to return the top three matches of the search based upon the hit-quality index (HQI) generated by the search routine. The top three hits were compared (Table 3) to the known identity of the feldspar phase as determined from previously published data, EMP or XRD analyses. The results (column 12 in Table 3) show that over 94% of the Raman spectra were correctly identified as the first choice HQI generated by SPECTRAL ID. In less than 5% of the spectra, the second choice HQI matched the correct phase, and in only one instance was the third choice HQI the correct phase. From this demonstration, we estimate that of the varieties of feldspars included in this study, the majority can be consistently and correctly classified into one of seven structural classes by a spectral searching and matching routine. The following exceptions exist: high albite cannot be distinguished from low albite, and shocked anorthite cannot be distinguished from anorthite-*I* and anorthite-*P*. A visual inspection of the Raman spectra of the albite samples (Fig. 6) does indicate that high albite can be easily distinguished visually from low albite on the basis of Raman band broadening and loss of secondary peaks. The same conclusion holds for distinguishing the shocked anorthite sample from crystalline anorthite. Perhaps the inclusion of more albite samples and anorthite spectra with higher signal-to-noise ratio will improve the capability to distinguish these varieties.

An additional use of the SPECTRAL ID program is the ability to identify and subtract out the Raman signal

of individual phases from a spectrum of a mixture of phases. Once a hit is generated for the major component in the spectrum of the mixture, the reference spectrum of that component can be subtracted from the recorded spectrum, and a new search performed to identify additional components. We have used this capability to identify two different phases occurring in the same area probed by the Raman laser beam, and the spectral database may be broadened to include reference Raman spectra of many other mineral types. This capability can be advantageous because the optics of a MMRS Raman system collects Raman scattering from fairly large fields of view ( $20\text{ }\mu\text{m}$  or larger), significantly increasing the chances for sampling several minerals.

We therefore conclude that ten major feldspar varieties can be identified by a careful visual inspection of the Raman spectrum, evaluation of their Raman peak positions, and by supplementing the analysis with a Raman spectrum database search-match routine such as that included in the SPECTRAL ID program. These ten feldspar varieties identifiable by Raman spectroscopy include: maximum microcline, orthoclase *s.s.*, sanidine, low albite, high albite, plagioclase, high anorthite-*I*, low anorthite-*P*, shocked anorthite, and ternary phases.

#### *Required performance of a field-based Raman system for identifying feldspars*

In order to distinguish feldspar minerals in the field solely on the basis of their Raman spectra, it is important to note a number of necessary requirements for instrumental performance of the field Raman system. Considering only the feldspar characterization, spectral information in the region  $150\text{ to }1500\text{ cm}^{-1}$  is all that is required. However, for distinguishing the feldspar minerals from other types of mineral, a Raman system covering the region  $150\text{ to }1800\text{ cm}^{-1}$  is all that is required. A strong case may be made (Wang *et al.* 2003), however, for an instrument also covering the additional spectral region from  $2500\text{ to }4000\text{ cm}^{-1}$ , which includes the OH-stretching bands of  $\text{H}_2\text{O}$ - and OH-bearing minerals, including the common products of alteration of feldspars, such as montmorillonite, scapolite, kaolinite, and zeolite.

A field Raman instrument capable of distinguishing the different feldspar phases must be able to determine Raman peak positions with an accuracy and precision of less than  $\pm 1\text{ cm}^{-1}$ . This degree of accuracy requires a field-calibration procedure to compensate for laser frequency-shifts arising from temperature variations and vibrations associated with mechanical transportation. This is especially true for unmanned deployments used in remote locations. In addition, large changes in the environmental temperature ( $\sim 10^\circ\text{C}$  or more) at a field site where the Raman spectra are being recorded will also require that the absolute wavenumber or wavelength scale of the CCD array camera be checked

at regular time-intervals and recalibrated as needed using an appropriate multi-line emission standard or a multi-band Raman standard sample. These precautions are necessary to keep the frequency errors in the Raman spectrum to less than  $\pm 1 \text{ cm}^{-1}$ . A spectrometer with a spectral resolution of at least  $4\text{--}5 \text{ cm}^{-1}$  is also needed to resolve and distinguish the narrow spectral peaks associated with the end members of the feldspars from the broadened Raman bands exhibited by disordered feldspars like sanidine, plagioclase, high albite, and shocked anorthite. Lastly, a beam size of the excitation laser with a focused diameter of  $<10 \text{ }\mu\text{m}$  is desirable to reduce the number of mineral phases in the excited volume of the sample. The MMRS that we have developed has the smallest spot-size ( $\sim 20 \text{ }\mu\text{m}$ ) among other available field Raman systems.

#### ACKNOWLEDGEMENTS

Some of the feldspar samples used in this investigation were provided by Drs. Guo Lihe of the Chinese Academy of Geological Sciences, Jill D. Pasteris, and Robert M. Dymek of Washington University in St. Louis. We very much appreciate these contributions. This work was partially supported by NASA grants NNG05GM95G (AW), NAG5-10703 (AW), and NAG5-12114(AW), and NNX07AQ34G (Mars Fundamental Research, BJ). Finally, we acknowledge two individuals who have inspired the work reported here. First is Dr. Joseph V. Smith, to whom this volume is dedicated. His focus on the feldspars over the years has been truly inspirational. We have spent many fond hours with *Feldspar Minerals* by J.V. Smith and the second edition, with W.L. Brown (Springer-Verlag 1974, 1988) and *Lunar Mineralogy, A Heavenly Detective Story* by J.V. Smith and I.M. Steele (*Am. Mineral.* **61**, 1976), to name just two. Second is our esteemed coauthor on this work, the late Dr. Larry A. Haskin. His dedication, like that of JVS, was an inspiration to us, and his untiring support of the development of laser Raman spectroscopy into a method for planetary surface exploration serves as strong motivation for us to continue this work until we achieve his dream of deploying a capable Raman system on the surface of another planet.

#### REFERENCES

- ARMSTRONG, J.T. (1988): Quantitative analysis of silicate and oxide materials: comparison of Monte Carlo, ZAF and  $\phi(\rho z)$  procedures. *Microbeam Analysis* **23**, 239-245.
- BANDFIELD, J.L. (2002): Global mineral distributions on Mars. *J. Geophys. Res.* **107**, 91/-920.
- BANDFIELD, J.L., HAMILTON, V.E. & CHRISTENSEN, P.R. (2000): A global view of martian surface compositions from MGS-TES. *Science* **287**(5458), 1626-1630.
- CHRISTENSEN, P.R., BANDFIELD, J.L., HAMILTON, V.E., RUFF, S.W., KIEFFER, H.H., TITUS, T.N., MALIN, M.C., MORRIS, R.V., LANE, M.D., CLARK, R.L., JAKOSKY, B.M., MELLON, M.T., PEARL, J.C., CONRATH, B.J., SMITH, M.D., CLANCY, R.T., KUZMIN, R.O., ROUSH, T., MEHALL, G.L., GORELICK, N., BENDER, K., MURRAY, K., DASON, S., GREENE, E., SILVERMAN, S. & GREENFIELD, M. (2001): Mars global surveyor thermal emission spectrometer experiment: investigation description and surface science results. *J. Geophys. Res.* **106**, 23823-23871.
- CHRISTENSEN, P.R., BANDFIELD, J.L., SMITH, M.D., HAMILTON, V.E. & CLARK, R.N. (2000): Identification of a basaltic component on the Martian surface from Thermal Emission Spectrometer data. *J. Geophys. Res.* **105**, 9609-9621.
- CLARK, B.C., MORRIS, R.V., MCLENNAN, S.M., GELLERT, R., JOLLIFF, B., KNOLL, A., SQUYRES, S.W., LOWENSTEIN, T.K., MING, D.W., TOSCA, N.J., YEN, A., CHRISTENSEN, P.R., GOREVAN, S., BRÜCKNER, J., CALVIN, W., DREIBUS, G., FARRAND, W., KLINGELHÖFER, G., WÄNKE, H., ZIPFEL, J., BELL, J., GROTZINGER, J., MCSWEEN, H.Y. & RIEDER, R. (2005): Chemistry and mineralogy of outcrops at Meridiani Planum, *Earth Planet. Sci. Lett.* **240**, 73-94.
- COONEY, T.F., SCOTT, E.R.D., KROT, A.N., SHARMA, S.K. & YAMAGUCHI, A. (1999): Vibrational spectroscopic study of minerals in the Martian meteorite ALH84001. *Am. Mineral.* **84**, 1579-1576.
- DANIEL, I., GILLET, P., McMILLAN, P.F. & RICHET, P. (1995a): An in situ high-temperature structural study of stable and metastable  $\text{CaAl}_2\text{Si}_2\text{O}_8$  polymorphs. *Mineral. Mag.* **59**, 25-33.
- DANIEL, I., GILLET, P., McMILLAN, P.F., WOLF, G. & VERHELST, M.A. (1997): High-pressure behavior of anorthite: compression and amorphization. *J. Geophys. Res.* **102**, 10,313-10,325.
- DANIEL, I., GILLET, P., POE, T.B. & McMILLAN, P.F. (1995b): In situ high-temperature Raman spectroscopic studies of aluminosilicate liquids. *Phys. Chem. Minerals* **22**, 74-86.
- DEER, W.A., HOWIE, R.A. & ZUSSMAN, J. (1991): *An Introduction to Rock-Forming Minerals* (2nd ed.). Pearson, Prentice Hall, New York, N.Y.
- DOWTY, E. (1987): Vibrational interactions of tetrahedra in silicate glasses and crystals: calculations on melilites, pyroxenes, silica polymorphs and feldspars. *Phys. Chem. Minerals* **14**, 122-138.
- DUNBAR, N.W. (1994): Crystallization processes of anorthoclase phenocrysts in the Mount Erebus magmatic system: evidence from crystal composition, crystal size distributions, and volatile contents of melt inclusions. In *Volcanological and Environmental Studies of Mount Erebus, Antarctica. Antarctic Research Series* **66**, 129-146.
- FARMER, V.C., ed. (1974): *The Infrared Spectra of Minerals*. Mineralogical Society, London, U.K.

- FROGNER, P., BROMAN, C. & LINDBLOM, S. (1998): Weathering detected by Raman spectroscopy using Al-ordering in albite. *Chem. Geol.* **151**, 161-168.
- GILLET, D.P., McMILLAN, P.F., WOLF, G. & VERHELST, M.A. (1977): High-pressure behavior of anorthite: compression and amorphization. *J. Geophys. Res.* **102**, 10313-10325.
- HASKIN, L.A., WANG, ALIAN, ROCKOW, K.M., JOLLIFF, B.L., KOROTOV, R.L. & VISKUPIC, K.M. (1997): Raman spectroscopy for mineral identification and quantification for in-situ planetary surface analysis: a point count method. *J. Geophys. Res.* **102**, 19293-19306.
- HEYMANN, D. & HÖRZ, F. (1990): Raman-spectroscopy and X-ray diffractometer studies of experimentally produced diaplectic feldspar glass. *Phys. Chem. Minerals* **17**, 38-44.
- JOLLIFF, B.L., FARRAND, W.H., JOHNSON, J.R., SCHRÖDER, C., WEITZ, C.M. & THE ATHENA SCIENCE TEAM (2006a): Origin of rocks and cobbles on the Meridiani Plains as seen by *Opportunity*. *Thirty-Seventh Lunar and Planetary Sci. Conf. (Houston)*, Abstr. **2401**.
- JOLLIFF, B.L. & HASKIN, L.A. (1995): Cogenetic rock fragments from a lunar soil: evidence of a ferroan noritic anorthosite pluton on the Moon. *Geochim. Cosmochim. Acta* **59**, 2345-2374.
- JOLLIFF, B.L., HUGHES, J.M., FREEMAN J.J. & ZEIGLER, R.A. (2006b): Crystal chemistry of lunar merrillite and comparison to other meteoritic and planetary suites of whitlockite and merrillite. *Am. Mineral.* **91**, 1583-1595.
- JOLLIFF, B.L., KOROTEV, R.L., ZEIGLER, R.A. & FLOSS, C. (2003): Northwest Africa 773: lunar mare breccia with a shallow-formed olivine-cumulate component, very-low-Ti (VLT) heritage, and a KREEP connection. *Geochim. Cosmochim. Acta* **24**, 4857-4879.
- KUEBLER, K.E., JOLLIFF, B.L., WANG, A. & HASKIN, L.A. (2006): Extracting olivine (Fo-Fa) compositions from Raman spectral peak positions. *Geochim. Cosmochim. Acta* **70**, 6201-6222.
- LARSEN, K.W., ARVIDSON, R.E., JOLLIFF, B.L. & CLARK, B.C. (2000): Correspondence and least squares analyses of soil and rock compositions for the Viking Lander 1 and pathfinder landing sites. *J. Geophys. Res.* **105**, 29207-29221.
- MATSON, D.W., SHARMA, S.K. & PHILPOTTS, J.A. (1986): Raman spectra of some tectosilicates and of glasses along the orthoclase-anorthite and nepheline-anorthite joins. *Am. Mineral.* **71**, 694-704.
- McKEOWN, D.A. (2005): Raman spectroscopy and vibrational analyses of albite: from 25°C through the melting temperature. *Am. Mineral.* **90**, 1506-1517.
- McMILLAN, P., PIRIOU, B. & NAVROTSKY, A. (1982): A Raman spectroscopic study of glasses along the joins silica – calcium aluminate, silica – sodium aluminate, and silica – potassium aluminate. *Geochim. Cosmochim. Acta* **46**, 2021-2037.
- McSWEEN, H.Y., ARVIDSON, R.E., BELL, J.F., III, BLANEY, D., CABROL, N.A., CHRISTENSEN, P.R., CLARK, B.C., CRISP, J.A., CRUMPLER, L.S., DES MARAIS, D.J., FARMER, J.D., GELLERT, R., GHOSH, A., GOREVAN, S., GRAFF, T., GRANT, J., HASKIN, L.A., HERKENHOFF, K.E., JOHNSON, J.R., JOLLIFF, B.L., KLINGELHOEFER, G., KNUDSON, A.T., MCLENAN, S., MILAM, K.A., MOERSCH, J.E., MORRIS, R.V., RIEDER, R., RUFF, S.W., DE SOUZA, P.A., JR., SQUYRES, S.W., WÄNKE, H. WANG, ALIAN, WYATT, M.B., YEN, A. & ZIPFEL, J. (2004): Basaltic rocks at the Spirit Landing Site in Gusev Crater. *Science* **305**, 842-845.
- MERNAGH, T.P. (1991): Use of the laser Raman microprobe for discrimination amongst feldspar minerals. *J. Raman Spectros.* **22**, 458-457.
- MING, D.W., MITTFELDELD, D.W., MORRIS, R.V., GOLDEN, D.C., GELLERT, R., YEN, A., CLARK, B.C., SQUYRES, S.W., FARRAND, W.H., RUFF, S.W., ARVIDSON, R.E., KLINGELHÖFER, G., McSWEEN, H.Y., RODIONOV, D.S., SCHRÖDER, C., DE SOUZA, P.A., JR. & WANG, ALIAN (2006): Geochemical and mineralogical indicators for aqueous processes in the Columbia Hills of Gusev Crater, Mars. *J. Geophys. Res.* **111** E02S12, doi:10.1029/2005JE002560.
- PAPIKE, J.J., KARNER, J.M. & SHEARER, C.K. (2003): Determination of planetary basalt parentage: a simple technique using the electron microprobe. *Am. Mineral.* **88**, 469-472.
- PURCELL, F.J. & WHITE, B. (1983): A Raman microprobe study of phase-separated minerals. *Microbeam Analysis*, 289-292.
- RIBBE, P.H. (1983a): Chemistry, structure and nomenclature of feldspars. In *Feldspar Mineralogy* (2<sup>nd</sup> ed., P.H. Ribbe, editor). *Rev. Mineral.* **2**, 1-19.
- RIBBE, P.H. (1983b): Aluminum-silicon order in feldspars; domain textures and diffraction patterns. In *Feldspar Mineralogy* (2<sup>nd</sup> ed., P.H. Ribbe, editor). *Rev. Mineral.* **2**, 21-54.
- RUBIN, A.E. (1997): Mineralogy of meteorite groups. *Meteoritics & Planet. Sci.* **32**, 231-247.
- RUFF, S.W. & CHRISTENSEN, P.R. (2002): Bright and dark regions on Mars: particle size and mineralogical characteristics based on thermal emission spectrometer data. *J. Geophys. Res.* **107**, 10/1-10/22.
- SALJE, E. (1986): Raman spectroscopic investigation of the order parameter behavior of hypersolvus alkali feldspar: displacive phase transition and evidence of Na-K site ordering. *Phys. Chem. Minerals* **13**, 340-346.
- SAUTTER, V., BARRAT, J.A., JAMBON, A., LORAND, J.P., GILLET, P., JAVOY, M., JORON, J.L. & LESOURD, M. (2002): A new Martian meteorite from Morocco: the nakhlite North West Africa 817. *Earth Planet. Sci. Lett.* **195**, 223-238.



- SCHRÖDER, C., RODIONOV, D.S., MCCOY, T.J., JOLLIFF, B.L., GELLERT, R., NITTLER, L.R.W., FARRAND, H., JOHNSON, J.R., RUFF, S.W., ASHLEY, J.W., MITTFELDELT, D.W., HERKENHOFF, K.E., FLEISCHER, I., HALDEMANN, A.F.S., KLINGELHÖFER, G., MING, D.W., MORRIS, R.V., DE SOUZA, P.A. JR., SQUYRES, S.W., WEITZ, C.A., YEN, S., ZIFFEL, J. & ECONOMOU, T. (2008): Meteorites on Mars observed with the Mars exploration rovers. *J. Geophys. Res.* **113**, E06S22, doi:10.1029/2007JE002990.
- SHARMA, S., SIMONS, B. & YODER, H.S., JR. (1983): Raman study of anorthite, calcium Tschermak's pyroxene, and gehlenite in crystalline and glassy states. *Am. Mineral.* **68**, 1113-1125.
- SMITH, J.V. & BROWN, W.L. (1988): *Feldspar Minerals. 1. Crystal Structures, Physical, Chemical and Microtextural Properties* (2<sup>nd</sup> ed.). Springer-Verlag, Berlin, Germany.
- SQUYRES, S.W., ARVIDSON, R.E., BLANEY, D.L., CLARK, B.C., CRUMPLER, L., FARRAND, W.H., GOREVAN, S., HERKENHOFF, K.E., HUROWITZ, J., KUSACK, A., MCSWEEN, H.Y., MING, D.W., MORRIS, R.V., RUFF, S.W., WANG, ALIAN & YEN, A. (2006): The rocks of the Columbia Hills. *J. Geophys. Res.* **111**, E02S11.
- TAYLOR, L.A., NAZAROV, M.A., SHEARER, C.K., MCSWEEN, H.Y., JR., CAHILL, J., NEAL, C.R., IVANOVA, M.A., BARSUKOVA, L.D., LENTZ, R.C., CLAYTON, R.N. & MAYEDA, T.K. (2002): Martian meteorite Dhofar: a new shergottite. *Meteoritics & Planet. Sci.* **37**, 1107-1128.
- VELDE, B. & BOYER, H.J. (1985): Raman spectra of naturally shocked microcline feldspar. *J. Geophys. Res.* **90**, 3675-3682.
- VELDE, B., SYONO, Y., KIKUCHI, M. & BOYER, H. (1989): Raman microprobe study of synthetic diaplectic plagioclase feldspars. *Phys. Chem. Minerals* **16**, 436-441.
- VON STENGEL, M.O. (1977): Normalschwingungen von Alkalifeldspäten. *Z. Kristallogr.* **146**, 1-18.
- WANG, ALIAN, HASKIN, L.A., LANE, A.L., WDOWIAK, T.J., SQUYRES, S.W., WILSON, R.J., HOVLAND, L.E., MANAIT, K.S., RAUF, N. & SMITH, C.D. (2003): Development of the Mars microbeam Raman spectrometer (MMRS). *J. Geophys. Res.* **108**, 5/1-5/18.
- WANG, ALIAN, JOLLIFF, B.L. & HASKIN, L.A. (1999): Raman spectroscopic characterization of a Martian SNC meteorite: Zagami. *J. Geophys. Res.* **104**, 8509-8519.
- WANG, ALIAN, JOLLIFF, B.L., HASKIN, L.A., KUEBLER, K.E. & VISKUPIC, K.M. (2001): Characterization and comparison of structural and compositional features of planetary quadrilateral pyroxenes by Raman spectroscopy. *Am. Mineral.* **86**, 790-806.
- WANG, ALIAN, KOROTEV, R.L., JOLLIFF, B.L., HASKIN, L.A., CRUMPLER, L., FARRAND, W.H., HERKENHOFF, K.E., DE SOUZA, P., JR., KUSACK, A.G., HUROWITZ, J.E. & TOSCA, N.J. (2006): Evidence of phyllosilicates in Woolly Patch, an altered rock encountered at West Spur, Columbia Hills, by the *Spirit* rover. *J. Geophys. Res.* **111**, E02S16.
- WANG, ALIAN, KUEBLER, K., JOLLIFF, B. & HASKIN, L.A. (2004a): Mineralogy of a Martian meteorite as determined by Raman spectroscopy. *J. Raman Spectros.* **35**, 504-514.
- WANG, ALIAN, KUEBLER, K., JOLLIFF, B. & HASKIN, L.A. (2004b): Raman spectroscopy of Fe-Ti-Cr-oxides, case study: martian meteorite EETA79001. *Am. Mineral.* **89**, 665-680.
- WHITE, E.B. (1974): Order disorder effects. In *The Infrared Spectra of Minerals* (V.C. Farmer, ed.). The Mineralogical Society, London, U.K. (87-110).
- XIROUCHAKIS, D., DRAPER, D.S., SCHWANDT, C.S. & LANZIOTTI, A. (2002): Crystallization conditions of Los Angeles, a basaltic Martian meteorite. *Geochim. Cosmochim. Acta* **66**, 1867-1880.
- YUND, R.A. & TULLIS, J. (1983): Subsolidus phase relations in the alkali feldspars with emphasis on coherent phases. In *Feldspar Mineralogy* (2<sup>nd</sup> ed., P.H. Ribbe, editor). *Rev. Mineral.* **2**, 203-220.
- ZOLTAI, T. & STOUT, J.H. (1984): *Mineralogy Concepts and Principles*. Burgess Publishing Co., Minneapolis, Minnesota.

Received October 11, 2007, revised manuscript accepted November 27, 2008.